nature neuroscience

Technical Report

https://doi.org/10.1038/s41593-025-01922-5

EPSILON: a method for pulse-chase labeling to probe synaptic AMPAR exocytosis during memory formation

Received: 13 September 2023

Accepted: 10 February 2025

Doyeon Kim[1], Pojeong Park[1,4], Xiuyuan Li[1,5], J. David Wong-Campos[1], He Tian[1], Eric M. Moult[1], Jonathan B. Grimm[2], Luke D. Lavis[2] & Adam E. Cohen[1,3]

A tool to map changes in synaptic strength during a defined time window could provide powerful insights into the mechanisms of learning and memory. Here we developed a technique, Extracellular Protein Surface Labeling in Neurons (EPSILON), to map α-amino-3-hydroxy-5-methyl-4-isoxazolepropionic acid receptor (AMPAR) exocytosis in vivo by sequential pulse-chase labeling of surface AMPARs with membrane-impermeable dyes. This approach yields synaptic-resolution maps of AMPAR exocytosis, a proxy for synaptic potentiation, in genetically targeted neurons during memory formation. In mice undergoing contextual fear conditioning, we investigated the relationship between synapse-level AMPAR exocytosis in CA1 pyramidal neurons and cell-level expression of the immediate early gene product cFos, a frequently used marker of engram neurons. We observed a strong correlation between AMPAR exocytosis and cFos expression, suggesting a synaptic mechanism for the association of cFos expression with memory engrams. The EPSILON technique is a useful tool for mapping synaptic plasticity and may be extended to investigate trafficking of other transmembrane proteins.

Changes in synaptic strength are an important component of learning and memory[1], but the rules that map a memory onto a specific set of synapses are not well understood. Which synapses represent which memories? How are changes in synaptic strength related to other markers of memory, such as expression of immediate early genes? To answer these questions, one would like a tool to map changes in synaptic strength during a defined time window in genetically defined neurons.

The synaptic density of α-amino-3-hydroxy-5-methyl-4-isoxazolepropionic acid receptors (AMPARs) is a major contributor to synaptic strength[2]. The density of AMPARs changes during long-term potentiation (LTP) via a combination of exocytosis and capture of laterally diffusing AMPARs[3,4]. AMPARs are stored in intracellular vesicles, which fuse with the postsynaptic membrane during LTP, exposing the N-terminal glutamate-binding domain to the extracellular space.

Several techniques have been developed for monitoring AMPAR dynamics in synapses in vivo. A fusion of the pH-sensitive Super Ecliptic pHluorin (SEP) to the N terminus of the AMPAR subunit GluA1 shows an increase in fluorescence when acidic AMPAR-containing vesicles fuse with the postsynaptic membrane[5]. The techniques of GFP reconstitution across synaptic partners (GRASP)[6], and its enhancement (eGRASP)[7], map synaptic contact area between genetically defined pairs of neurons. A related technique, called synaptic proximity ligation

---

[1]Department of Chemistry and Chemical Biology, Harvard University, Cambridge, MA, USA. [2]Janelia Research Campus, Howard Hughes Medical Institute, Ashburn, VA, USA. [3]Department of Physics, Harvard University, Cambridge, MA, USA. [4]Present address: Department of Brain Sciences, DGIST, Daegu, Republic of Korea. [5]Present address: Department of Applied Biology and Chemical Technology, Hong Kong Polytechnic University, Kowloon, Hong Kong. e-mail: cohen@chemistry.harvard.edu

assay (SYNPLA), maps AMPAR density in synapses between genetically defined pairs of neurons[8]. Finally, a technique to biotinylate surface-exposed AMPARs has been used to track their lateral diffusion in vivo[9]. However, no technique has yet been able to identify all the potentiated synapses in a defined neuron, time window and arbitrary brain location (for example, one that is too deep to image in real-time via a cranial window).

Protein labeling with HaloTag ligand (HTL) dyes has been used to probe protein turnover at the level of translation and degradation in vivo[10,11]. A fusion of a target protein and the HaloTag receptor (HT) can be covalently and irreversibly labeled with a fluorescent HTL dye. A technique called DELTA (Dye Estimation of the Lifetime of proTeins in the brAin) used saturated labeling of an HT fusion to a target protein with one dye color (pulse), and subsequent labeling of newly synthesized proteins with different colors (chase), to map protein synthesis in vivo, with an ex vivo readout[11]. Since the dyes used in DELTA were membrane permeable, this technique was not sensitive to membrane trafficking, but only to total protein level.

Here, we developed an approach to map AMPAR insertion by pulse-chase labeling of surface AMPARs with membrane-impermeable fluorescent dyes. We call the technique EPSILON. We fused an HT to the N terminus of GluA1 (Fig. 1a). We expressed HT-GluA1 in neurons, and then saturated surface-exposed HT-GluA1 via direct brain injection of a membrane-impermeable HTL dye. A second dye of a different color was then added to label newly surface-exposed HT-GluA1, and the animal was exposed to a variety of learning paradigms (Fig. 1b). Subsequent ex vivo multi-color imaging revealed maps of AMPAR exocytosis with single-synapse resolution across large volumes of brain tissue and in multiple brain regions.

We went on to map synaptic plasticity and cFos expression in hippocampal CA1 pyramidal cells upon contextual fear conditioning (CFC). In mice subjected to CFC, but not in controls, we observed a tight correlation between the degree of synaptic plasticity and the cFos expression level. This finding suggests a synaptic mechanism for the observed association of cFos expression with memory engrams. We also observed more plasticity in perisomatic than in distal synapses, and clusters of plasticity among nearby synapses. These features may reflect interactions between plasticity and dendritic excitability properties[12]. Overall, EPSILON tagging of AMPAR exocytosis is a powerful tool to investigate the distribution and time course of synaptic plasticity, and we expect that the EPSILON approach could be applied to other transmembrane proteins.

Results

Development of EPSILON and validation in cultured neurons

We replaced the pH-sensitive SEP domain in SEP-GluA1 with HT to create HT-GluA1. This design used a flexible glycine linker between HT and GluA1 and retained the N-terminal GluA1 signal peptide[13] to ensure proper protein trafficking[5].

We first tested the EPSILON labeling scheme in cultured rat hippocampal neurons. We characterized (1) expression and trafficking of HT-GluA1, (2) the labeling kinetics of membrane-impermeable HTL dyes and (3) the turnover rate of surface HT-GluA1. Live-cell labeling with a membrane-impermeable dye selectively tagged the surface-exposed HT-GluA1 receptors (Extended Data Fig. 1a). Surface-labeled HT-GluA1 strongly colocalized with the postsynaptic density marker PSD95.FingR-eGFP[14] (Manders' overlap coefficient 0.87 ± 0.025, mean ± s.e.m., $n = 13$ dendrites from 7 neurons; Fig. 1c and Extended Data Fig. 1b). The subcellular distribution of HT-GluA1 labeled with a permeable HTL dye (JF_{549}) strongly correlated with the distribution of all GluA1 as reported by anti-GluA1 immunostaining (Pearson's $R = 0.73$, $P < 10^{-4}$, $n = 32$ spines, 5 neurons; Extended Data Fig. 1c,d). Anti-GluA1 immunostaining showed no difference in total GluA1 between cells ± HT-GluA1 expression (Extended Data Fig. 1e). Together, these measurements indicated that the surface-exposed and intracellular pools of HT-GluA1 followed close-to-native trafficking patterns.

Pulse labeling of surface HT-GluA1 reached steady state after approximately 300 s for AF_{488} (100 nM), 60 s for JF_{549i} (ref. 15) (1 µM) and 60 s for Alexa Fluor 647 (AF_{647}) (1 µM; see Methods for synthesis of AF_{647}-HTL; Extended Data Fig. 1f–i). Subsequent chase labeling with a different-colored impermeable dye showed no additional labeling (Extended Data Fig. 1j–o), indicating that the pulse had saturated the surface-exposed HT receptors. In subsequent pulse-chase labeling experiments in cultured neurons, we used conditions that saturated labeling (AF_{488}: 100 nM for 5 min; JF_{549i}: 1 µM for 60 s; AF_{647}: 1 µM for 60 s).

We next determined the basal turnover rate of surface HT-GluA1 (Extended Data Fig. 1p–r) by pulsing with AF_{488}, and then chasing with JF_{549i} after a variable delay. The ratio of the pre-existing (labeled with AF_{488}) and newly inserted (labeled with JF_{549i}) surface HT-GluA1 yielded the turnover rate. The half-life of surface HT-GluA1 was approximately 30 min in cultured neurons.

We then asked whether pulse-chase labeling of surface HT-GluA1 could serve as a proxy of synaptic potentiation. We saturated the surface HT-GluA1 with Dye 1 (AF_{647}), washed out unreacted dye and then induced structural LTP in individual spines via focally targeted pulsed glutamate uncaging (60 pulses at 1 Hz) in Mg^{2+}-free solution (Methods and Fig. 1d)[16]. Glutamate uncaging triggered rapid spine growth followed by slight shrinkage (Extended Data Fig. 2a,b), as previously reported[16]. Spine growth trajectories were indistinguishable between neurons ± HT-GluA1 expression (Extended Data Fig. 2b), indicating that HT-GluA1 expression did not perturb structural plasticity. We then stained the cells with Dye 2 (JF_{549i}) to label the freshly exocytosed HT-GluA1, and performed high-resolution three-color confocal imaging of a nonspecific membrane marker (GPI-eGFP), Dye 1 and Dye 2. The spines exposed to glutamate uncaging showed increased spine size (measured by GFP fluorescence, indicating structural LTP), increased Dye 1 signal (likely indicating recruitment of pre-existing surface-exposed HT-GluA1 by lateral diffusion) and increased Dye 2 (indicating freshly exocytosed HT-GluA1; Fig. 1e–h and Extended Data Fig. 2c,d). Finally, the labeling levels of Dye 1 and Dye 2 correlated with the increase in spine size on a spine-by-spine basis (Fig. 1i and Extended Data Fig. 2e). These results indicate that Dye 2 was a robust proxy for LTP at the single-spine level.

We further validated the EPSILON technique via glycine-induced chemical LTP (cLTP) in cultured neurons (Methods)[17]. We saturated the surface HT-GluA1 with Dye 1 (AF_{647}), induced cLTP and then stained with Dye 2 (JF_{549i}) to label the newly exocytosed HT-GluA1 (Fig. 1j–n and Extended Data Fig. 2f,g). The slope of the plot of Dye 2 versus Dye 1 in cLTP-treated neurons was twofold higher compared with controls (cLTP: 0.15 ± 0.01, $n = 47{,}090$ spines; control: 0.076 ± 0.008, $n = 32{,}828$ spines; $P = 0.0001$; Fig. 1k,m,n). We also observed a significantly larger fraction of spines highly labeled with Dye 2 in cLTP-treated neurons compared with controls (Fig. 1l and Extended Data Fig. 2f,g; cLTP: 1,024 of 47,090 spines above threshold (2.2%), $n = 44$ neurons, 6 dishes; control: 195 of 32,828 spines above threshold (0.6%), $n = 54$ neurons, 6 dishes; $P = 0.043$, two-sided Student's t-test). Co-transduction with tetanus toxin light chain (TeTX-LC)[3] blocked the increase in the fitted slope upon cLTP treatment and reduced the fraction of spines above threshold, implying that both parameters depend on AMPAR exocytosis (Fig. 1k–n and Extended Data Fig. 2f,g; TeTX-LC: slope = 0.086 ± 0.009; 35 of 17,231 spines above threshold (0.2%); $n = 45$ neurons, 6 dishes). This analysis revealed that cLTP induced both an increase in the fraction of spines undergoing AMPAR exocytosis and also an increase in the amount of exocytosis in each spine.

Validation of EPSILON in barrel cortex, in vivo

To characterize HT-GluA1 in the live mouse brain, we coexpressed HT-GluA1 and myc-GluA2 in layer 2/3 neurons in mouse barrel cortex

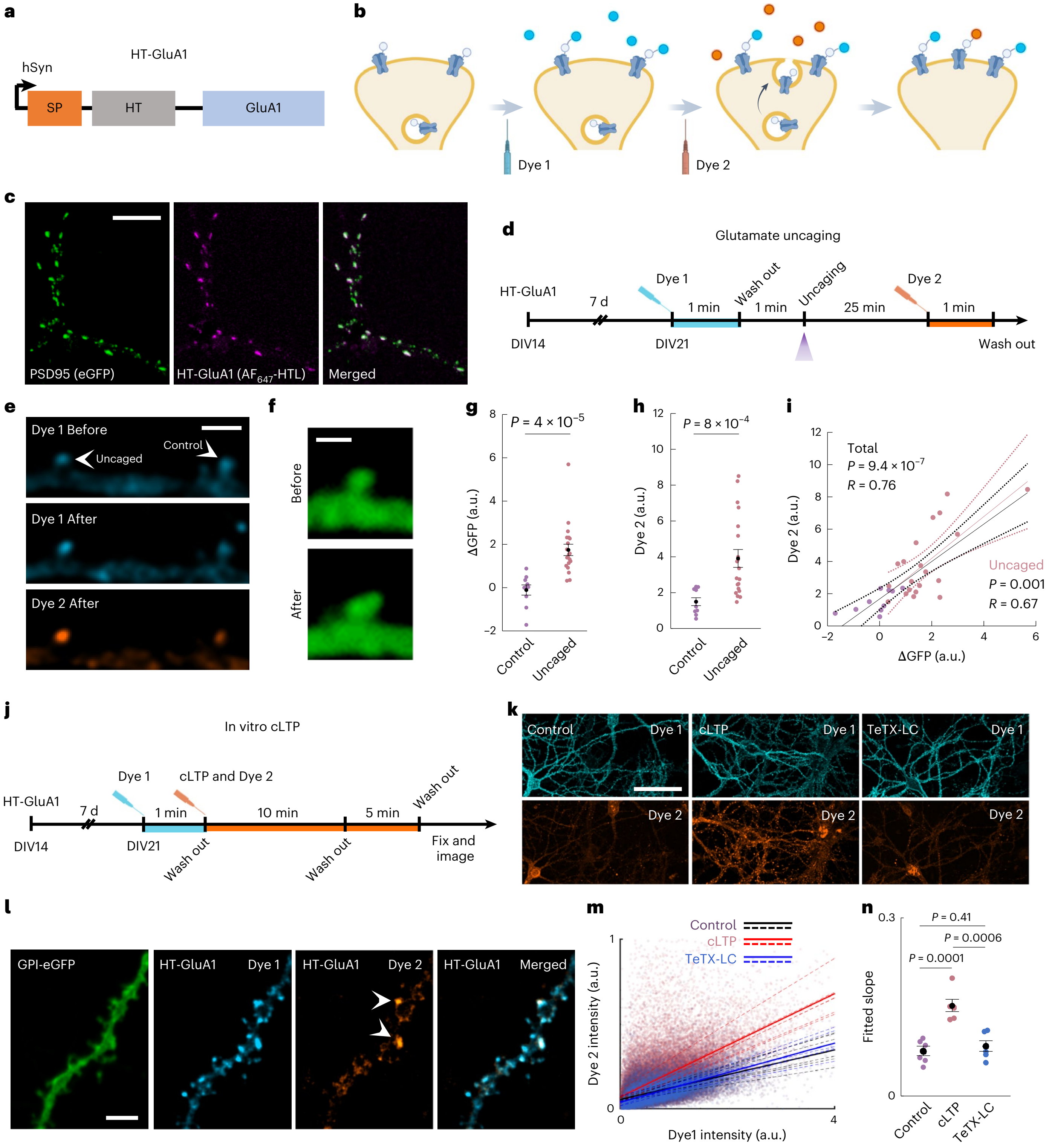

Fig. 1 | EPSILON tags freshly exposed AMPARs. **a**, Composition of HT-GluA1. **b**, EPSILON scheme for labeling freshly surface-exposed AMPARs using membrane-impermeable dyes. Dye 1 saturates HT labeling sites on pre-existing surface-exposed HT-GluA1. Dye 2 tags newly exocytosed HT-GluA1. **c**, HT-GluA1 localization in a neuron. Left: PSD95 (PSD95.FingR-eGFP); middle: HT-GluA1 (AF$_{647}$-HTL); right: merge. Scale bar, 10 µm. Micrographs represent one of three independent experiments. **d**, Timeline for pulse-chase labeling during glutamate photo-uncaging. **e**, Glutamate uncaging triggers AMPAR exocytosis. Top: pre-existing HT-GluA1 (Dye 1); middle: Dye 1 after uncaging; bottom: newly exposed HT-GluA1 (Dye 2). Scale bar, 2 µm. **f**, Dendritic spine in GPI-eGFP-labeled neuron before (top) and after (bottom) uncaging. Scale bar, 1 µm. **g**,**h**, Glutamate uncaging induced spine growth (**g**) and increased Dye 2 labeling (**h**). Control: $n = 10$ spines; uncaged: $n = 20$ spines. Two-sided Wilcoxon rank-sum test. Error bars, mean ± s.e.m. **i**, Correlation between Dye 2 intensity and spine size change (R, Pearson's correlation; P, Student's t-test). Dashed lines indicate 95% confidence intervals on the fits. **j**, Timeline for pulse-chase labeling during cLTP. **k**, Spine labeling for control, cLTP and TeTX-LC groups. Top: pre-existing HT-GluA1 (Dye 1). Bottom: newly exposed HT-GluA1 (Dye 2). Scale bar, 10 µm. **l**, Spines with elevated HT-GluA1 exocytosis evoked by cLTP. Arrowheads indicate spines with high HT-GluA1 exocytosis. Scale bar, 5 µm. **m**, cLTP increased Dye 2/Dye 1 ratios. Control: $n = 32{,}828$ spines; cLTP: $n = 47{,}090$; TeTX-LC: $n = 17{,}231$ (6 cultures each). Outliers are shown in Extended Data Fig. 2f. **n**, Slopes from **m**. Two-sided Student's t-test. Error bars, mean ± s.e.m. Schematics in **a**, **d** and **j** created using BioRender.com. SP, GluA1 signaling peptide.

via in utero electroporation (IUE) (Fig. 2a). As in previous experiments with SEP-GluA1, we used a 1:1 ratio of HT-GluA1 and myc-GluA2 to maintain the endogenous subunit stoichiometry[5]. In some experiments, we coexpressed a membrane marker, GPI-eGFP, and verified that HT-GluA1 was well trafficked at morphologically defined spines (Fig. 2a). In separate experiments, we coexpressed a spine marker, PSD95.FingR-eGFP, and verified HT-GluA1 co-localization with molecularly defined spines (Extended Data Fig. 3a–g). In acute brain slices, patch-clamp recordings with extracellular stimulation of excitatory synaptic inputs showed that HT-GluA1/myc-GluA2 expression did not significantly alter AMPAR-mediated excitatory postsynaptic currents (EPSCs) or the AMPAR/*N*-methyl-D-aspartate receptor (NMDAR) ratio (Fig. 2b–e). Current-clamp experiments confirmed that HT-GluA1/myc-GluA2 expression also did not significantly alter membrane resistance, membrane capacitance, resting potential, rheobase or excitability (Extended Data Fig. 3h,i). The expression of HT-GluA1/myc-GluA2 also did not change the density of spines on dendrites (Extended Data Fig. 3j,k) or the total GluA1 expression level as assessed by anti-GluA1 antibody staining (Extended Data Fig. 3l,m).

To quantify basal turnover of AMPARs (that is, replacement of surface-exposed molecules with fresh ones from vesicles), we performed pulse-chase labeling of surface HT-GluA1 in the barrel cortex in vivo (Fig. 2f, Extended Data Fig. 4a,b and Methods). We first verified by GFAP staining that repeated dye injections did not activate an inflammatory response (Extended Data Fig. 4c). We then saturated pre-existing surface HT-GluA1 by intracortical injection of Dye 1 (1.4 µl of 1 µM AF_{647}; Extended Data Fig. 4d,e). After 20 min—enough time for Dye 1 to react—we injected Dye 2 (1.4 µl of 10 µM JF_{549i}) at the same sites with tenfold higher concentration to ensure that most new HT-GluA1 was labeled with Dye 2 and not residual Dye 1. The mice were returned to their home cage, except for those with an interinjection delay of 0.3 h, and after a variable delay, we injected Dye 2 again to ensure complete labeling of newly surface-exposed HT-GluA1. Confocal images of fixed brain sections mapped both dyes throughout $1.2–4.6 \times 10^5$ spines in three mice at each time point (Fig. 2g), and the fluorescence intensities were quantified for each spine (Fig. 2h). The half-life for surface HT-GluA1 on spines in vivo was approximately 50 h (Fig. 2i). The disparity in surface lifetime between culture (30 min) and in vivo (50 h) is consistent with earlier reports which showed an acceleration of GluA1 protein turnover in slice cultures versus in vivo[18,19]. Pulse-chase experiments on timescales shorter than ~50 h could thus identify spines with accelerated AMPAR exocytosis. We also validated that the background autofluorescence and residual dyes contributed negligible fluorescence signal (Extended Data Fig. 4f,g and Supplementary Information).

The adult barrel cortex exhibits synaptic plasticity in response to changes in sensory experience, such as stimulation or deprivation of a subset of whiskers[5,20]. To tag spines with elevated GluA1 exocytosis upon acute sensory stimulation, we performed EPSILON labeling while stimulating a subset of whiskers in an anesthetized mouse (Fig. 2j, Extended Data Fig. 4b and Methods). Confocal images of layer 2/3 pyramidal neurons in fixed brain sections from the contralateral barrel cortex displayed spines with elevated Dye 2 (AF_{488}), indicative of newly surface-exposed HT-GluA1 (Fig. 2k). Mice subjected to whisker stimulation had a larger fraction of spines with elevated Dye 2 compared with controls (whisker-stimulated: 1.1 ± 0.34%, mean ± s.e.m., over 4 mice ($n = 203{,}787$ spines); control: 0.27 ± 0.11%, over 3 mice ($n = 117{,}829$ spines); Fig. 2l–n and Supplementary Information). These findings demonstrate that pulse-chase HT-GluA1 AMPAR labeling can tag individual spines that undergo elevated AMPAR exocytosis in vivo.

Hippocampal plasticity and cFos in fear conditioning

The CA1 region of the hippocampus is involved in formation and storage of context-related memories[21], but the physical nature of the hippocampal engram, or memory trace, remains unclear. On one hand, activation of subsets of hippocampal cells, termed engram neurons, is necessary and sufficient to recreate simple conditioned responses (for example, freezing after CFC)[22]. These cells are often identified using expression of immediate early genes (for example, *FOS*)[23]. On the other hand, modulation of synaptic strength is also necessary for memory formation[24]. The relation between synapse-level and cell-level memory encodings is unclear[25].

We used HT-GluA1 to investigate the relation between AMPAR exocytosis and cFos expression in hippocampal CA1 pyramidal cells upon CFC. We expressed HT-GluA1/myc-GluA2 via IUE in hippocampal CA1 pyramidal neurons (Methods). As in the cortex, HT-GluA1 localized to dendritic spines (Fig. 3a). We then used EPSILON tagging followed by fixed slice imaging to map newly exocytosed AMPARs in mice that underwent CFC, home cage control mice, and mice that were exposed to the context but not the conditioned stimulus (foot shock) (Fig. 3b and Extended Data Figs. 4b and 5a)[26]. For each pyramidal neuron expressing HT-GluA1, we located every spine and quantified the fluorescence of Dye 1 and Dye 2 (Supplementary Information). We also quantified endogenous cFos in the nucleus via immunofluorescence in a third spectral channel (Extended Data Fig. 5b–e).

As in the barrel cortex, a subset of spines had elevated Dye 2 (JF_{549i}) fluorescence, indicative of AMPAR exocytosis (Fig. 3c,d). We quantified the fraction of spines with elevated Dye 2 for each neuron (Fig. 3e–h). The mean fractions of potentiated spines per neuron were not significantly different between the CFC and context-only groups, but both groups were significantly higher than in the home cage control group (CFC: 1.6 ± 0.27%, mean ± s.e.m., $n = 75{,}200$ spines, 19 cells, 4 mice; context-only: 0.94 ± 0.09%, $n = 100{,}534$ spines, 23 cells, 6 mice; home cage control: 0.36 ± 0.06%, $n = 43{,}659$ spines, 12 cells, 3 mice; Fig. 3i). In the CFC mice, a subset of neurons had an elevated fraction of potentiated spines compared with context-only controls (7 of 19 neurons in CFC mice had a higher fraction of potentiated spines than all 23 neurons from context-only controls; Fig. 3i). Furthermore, the Dye 2 fluorescence in potentiated spines in the CFC group was brighter than in either the home cage control or the context-only group (CFC: 1,000 ± 35 counts, mean ± s.e.m., $n = 1{,}016$ spines from 19 cells, 4 mice; context-only: 906 ± 35 counts, $n = 811$ spines from 22 cells, 4 mice, $P = 0.0075$; home cage control: 789 ± 36 counts, $n = 215$ spines from 12 cells, 3 mice, $P = 0.002$; Fig. 3j). Finally, within the CFC group, the level of Dye 2 in potentiated spines correlated with the fraction of potentiated spines on a cell-by-cell basis ($R = 0.48$, $P = 0.04$; Extended Data Fig. 6a). These results imply that the conditioned stimulus elevated the percentage of potentiated spines and the degree of AMPAR exocytosis in a subset of neurons.

We next compared AMPAR exocytosis and cFos expression at the level of individual cells (Fig. 3k–o and Extended Data Fig. 6b). Mice exposed to CFC had more cFos expression compared with either context-only or home cage controls (CFC: cFos level $1.1 \times 10^4 \pm 1.1 \times 10^2$ a.u., mean ± s.e.m., $n = 7{,}208$ cells, 4 mice; context-only: $6.7 \times 10^3 \pm 94$ a.u., $n = 6{,}407$ cells, 6 mice; home cage control: $5.8 \times 10^3 \pm 1.3 \times 10^2$ a.u., $n = 1{,}922$ cells, 3 mice; Fig. 3m and Extended Data Fig. 5b–e), consistent with previous reports[27]. We plotted the fraction of spines with high AMPAR exocytosis as a function of the cFos expression, cell by cell. These two quantities were highly correlated within the CFC group ($R = 0.90$, $P < 0.0001$), but not in the context-only group, nor in the home cage control group (Fig. 3n,o). To rule out imaging artifacts, we verified that the fraction of potentiated spines, the cFos intensity and the total number of detected spines were independent of the imaging depth below the slice surface in either the CFC or context-only groups (Extended Data Fig. 6c–e). Moreover, the total number of spines (labeled with Dye 1) did not correlate with cFos intensity (Extended Data Fig. 6f). Together, these results establish that during the formation of associative memory, CA1 neurons with higher activity (as reported by cFos) exhibited higher AMPAR exocytosis compared with low-cFos neurons from the same animal.

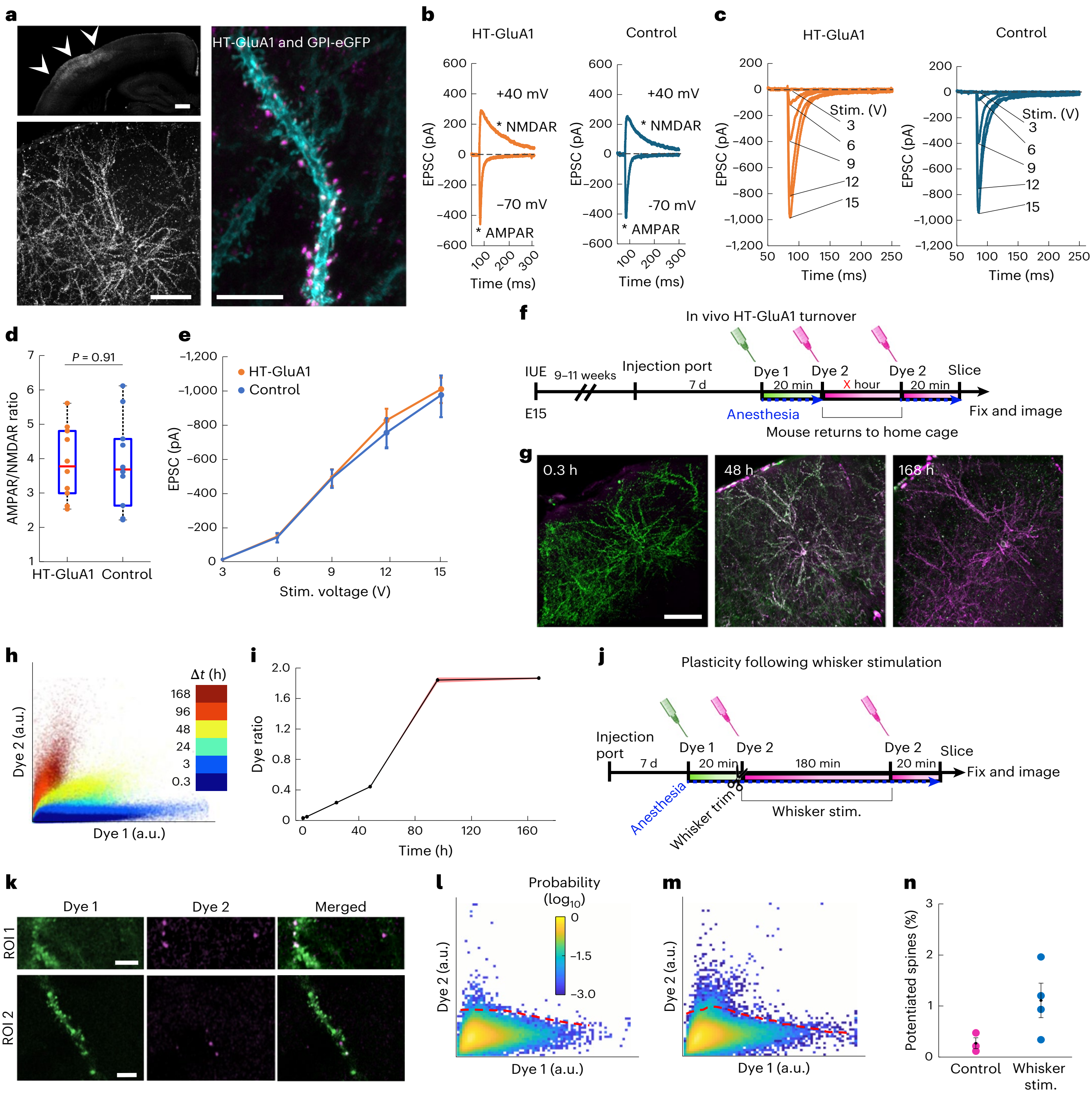

Fig. 2 | EPSILON reports sensory-induced AMPAR exocytosis in vivo. **a**, HT-GluA1 expression in mouse barrel cortex layer 2/3 pyramidal neurons (fixed slice). Top left: coronal section. Arrowheads: barrel cortex. Bottom left: HT-GluA1-expressing neurons. Right: dendrite coexpressing eGFP (cyan) and HT-GluA1 (AF_{647}-HTL, magenta). Scale bars, 500 µm (top left), 200 µm (bottom left), 10 µm (right). **b**, AMPAR and NMDAR components of EPSCs in layer 2/3 pyramidal neurons. **c**, AMPAR-mediated EPSCs with varying stimulus intensities. **d**, AMPAR/NMDAR ratio in HT-GluA1-expressing and control neurons (*n* = 10 neurons per group). Box plot shows extrema, 25th and 75th percentiles and median. Two-sided Wilcoxon rank-sum test. **e**, AMPAR EPSC amplitude versus electric field stimulus strength (*n* = 10 neurons per group). Error bars, mean ± s.e.m. **f**, EPSILON pulse-chase scheme for mapping turnover of surface AMPARs in vivo. **g**, HT-GluA1 in layer 2/3 barrel cortex at 0.3, 48 and 168 h after the first chase. Green, Dye 1 (AF_{647}); magenta, Dye 2 (JF_{549i}). Scale bar, 200 µm. **h**, Spine fluorescence scatterplots at intervals after the first chase (*n* = 3 mice per interval; total spines: 0.3 h = 312,246, 3 h = 164,403, 24 h = 458,181, 48 h = 340,927, 96 h = 26,765, 168 h = 121,503). **i**, Slopes from **h** via least-squares regression. Red-shaded error band, mean slope ± 95% confidence interval. **j**, EPSILON scheme for sensory-evoked AMPAR exocytosis. **k**, Spines labeled during whisker stimulation. Left: pre-existing (Dye 1, JF_{549i}); middle: newly exocytosed (Dye 2, AF_{488}); right: merge. Scale bar, 5 µm. **l**,**m**, Density plot of spine fluorescence in control mice (**l**) (*n* = 117,829 spines, 3 mice) and in whisker-stimulated mice (**m**) (*n* = 203,787 spines, 4 mice). Dashed lines: thresholds (Supplementary Information). **n**, Fraction of spines above Dye 2 intensity threshold (control: *n* = 3 mice; stimulated: 4 mice). Each data point indicates one mouse. Error bars, mean ± s.e.m. Schematics in **f** and **j** created using BioRender.com. E15, embryonic day 15; ROI, region of interest; stim., stimulated.

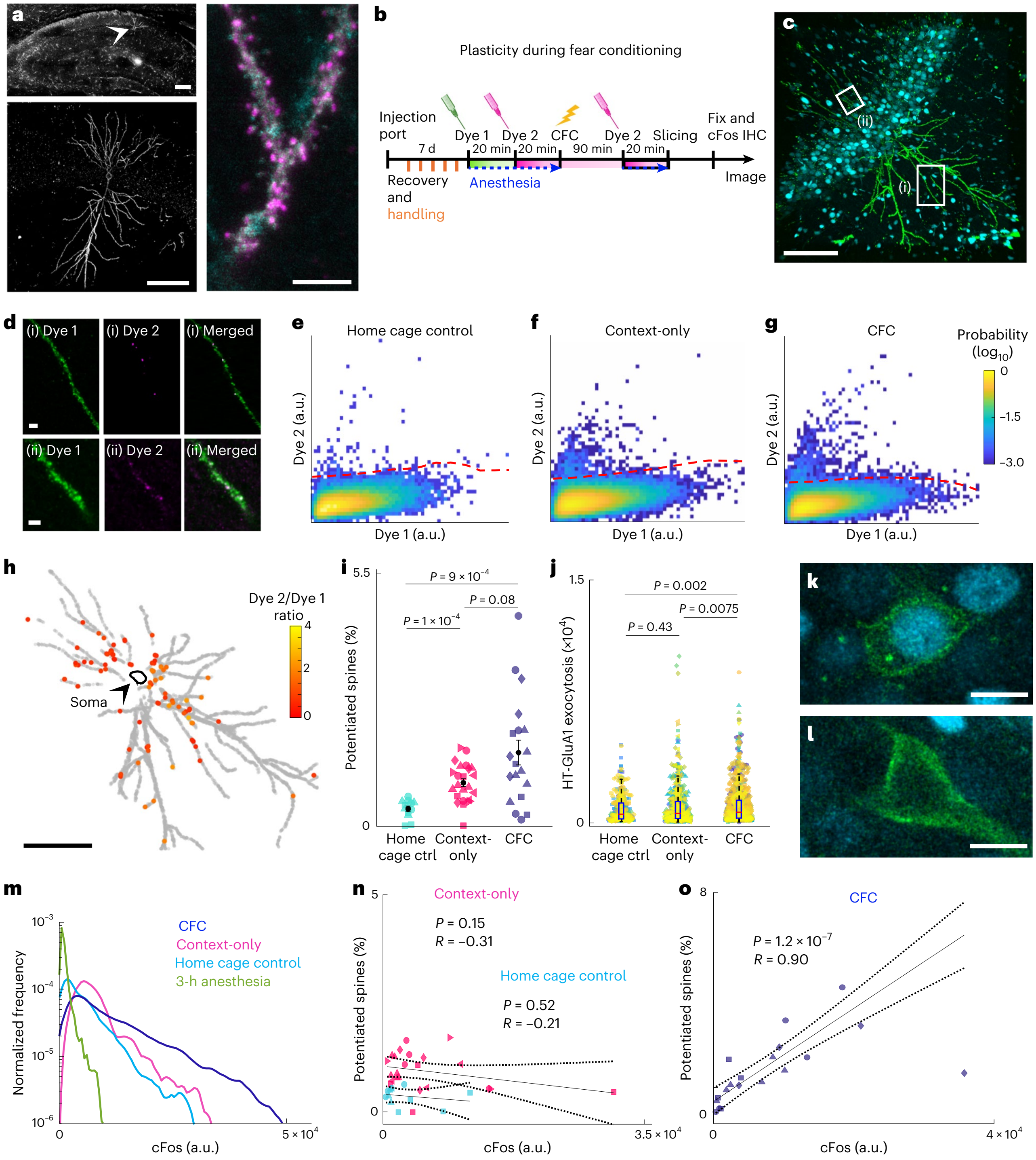

Fig. 3 | CFC evokes correlated changes in AMPAR exocytosis and cFos expression. a, HT-GluA1 expression in mouse hippocampus CA1 pyramidal neurons (fixed slice). Top left: coronal section. Bottom left: HT-GluA1-expressing single neuron. Right: dendrites coexpressing membrane-localized eGFP (cyan) and HT-GluA1 (AF_{647}-HTL, magenta). Arrowhead indicates an expressing cell. Scale bars, 200 µm (top left, bottom left), 5 µm (right). **b**, EPSILON scheme for tagging spines potentiated during CFC. **c**, CA1 neuron after EPSILON tagging, CFC and cFos immunostaining. Pre-existing HT-GluA1 (green) and cFos (cyan). Scale bar, 200 µm. **d**, Insets from **c** showing pre-existing HT-GluA1 (Dye 1, AF_{647}) and newly exposed HT-GluA1 (Dye 2, JF_{549i}). Scale bar, 10 µm. **e**–**g**, Density plots of spine fluorescence in home cage control (**e**), context-only (**f**) and CFC (**g**) animals. Thresholds are indicated with dashed lines (Supplementary Information). Home cage control: $n = 43{,}659$ spines, 3 mice; context-only: 100,534 spines, 6 mice; CFC: 75,200 spines, 4 mice. **h**, Map of spines with Dye 2/Dye 1 above threshold. Scale bar, 200 µm. **i**, Percentage of spines above Dye 2 threshold. Home cage: $n = 12$ cells, 3 mice; context-only: 23 cells, 6 mice; CFC: 19 cells, 4 mice. Error bars, mean ± s.e.m.; two-sided Wilcoxon rank-sum test. Distinct mice are indicated by different shape symbols. **j**, Dye 2 intensity in potentiated spines. Home cage: $n = 215$ potentiated spines, 12 cells, 3 mice; context-only: 811 potentiated spines, 22 cells, 6 mice; CFC: 1,016 potentiated spines, 19 cells, 4 mice. Box plot shows extrema, 25th and 75th percentiles and median. Distinct mice are indicated with marker shape and distinct cells by marker color. **k**,**l**, CA1 neurons expressing HT-GluA1 (green) with high (**k**) or low (**l**) cFos expression (cyan). Scale bars, 10 µm. **m**, cFos intensity distributions: no exposure (2,285 cells, 3 mice), home cage (1,922 cells, 3 mice), context-only (6,407 cells, 6 mice), CFC (7,208 cells, 4 mice). **n**,**o**, Cell-by-cell correlation between cFos intensity and fraction of spines with high HT-GluA1 exocytosis: home cage (12 cells, 3 mice), context-only (23 cells, 6 mice) (**n**); CFC (19 cells, 4 mice) (**o**). Dashed lines in **n** and **o** indicate 95% confidence intervals on the fits. *R*, Pearson's correlation; *P*, two-sided Student's *t*-test. Schematic in **b** created using BioRender.com. Ctrl, control; IHC, immunohistochemistry.

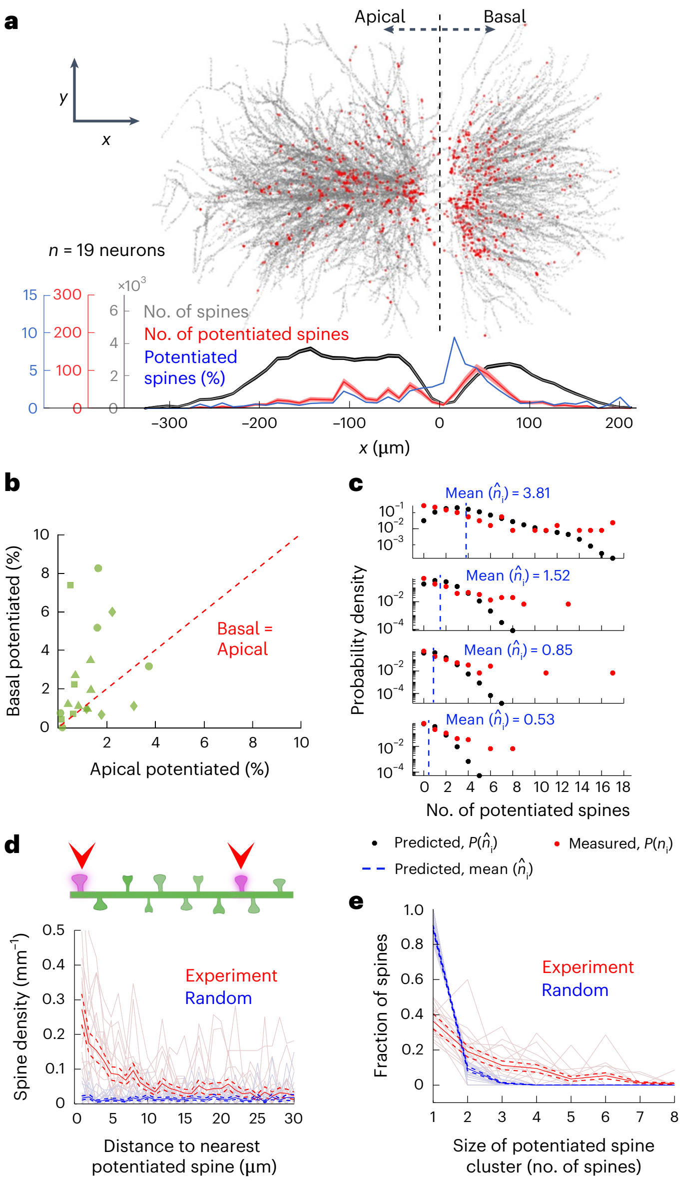

Fig. 4 | Subcellular distribution of AMPAR exocytosis after CFC in CA1 pyramidal neurons. a, Distribution of spines with high HT-GluA1 exocytosis as a function of distance from the stratum pyramidale. Top: overlapped images of all identified spines (gray) and spines with high HT-GluA1 exocytosis (red). Bottom: density profiles of all spines (gray), potentiated spines (red) and fraction of potentiated spines (blue). Shading represents count ± square root (count). **b**, Fraction of potentiated spines in basal versus apical dendrites in neurons. Each shape represents a different animal. **c**, Distributions of the measured (n_i) and predicted ($\hat{n}_i$) number of potentiated spines in individual dendrite segments from the CFC group ($n = 1{,}476$ dendrite segments, 19 neurons). $P(\hat{n}_i)$ was evaluated from 500 random allocations of potentiated spines among dendrites of a given branch order within each cell. The plots show distributions for groups of dendritic segments with similar $\langle \hat{n}_i \rangle$ (regardless of branch order) and sorted by decreasing mean $\hat{n}_i$ from top to bottom. **d**, Density profile of potentiated spines as a function of distance from the nearest potentiated spine. The single-cell profiles are plotted with light colors. Bold and dashed lines represent mean ± s.e.m. Random: simulation where the same number of potentiated spines was distributed randomly and independently among all detected spines. Arrowheads indicate potentiated spines. **e**, Fraction of potentiated spine clusters of different sizes. The single-cell profiles are plotted with light colors. Bold and dashed lines represent mean ± s.e.m. Random defined as in **d**. All data from $n = 19$ neurons, 4 mice, subjected to CFC. Schematic in **d** created using BioRender.com.

Mapping subcellular patterns of plasticity

We then analyzed the subcellular distributions of spines with high AMPAR exocytosis. We segmented the dendrites and registered all spines to their corresponding dendrites (Extended Data Fig. 7a,b). AMPAR exocytosis was more prevalent in perisomatic than in distal spines (Fig. 4a and Extended Data Fig. 7c–i), with a bias toward basal over apical dendrites (Fig. 4b and Extended Data Fig. 8a–d). We did not observe any difference in the spatial distribution of AMPAR exocytosis between CFC versus control mice, nor between high- and low-cFos-expressing cells within each experimental group (Extended Data Fig. 8e–g).

We next sought to assess whether individual dendritic segments had either an excess or deficit in number of potentiated spines. To remove the overall dependence of exocytosis on distance from the soma, we compared dendrites of equal branch order. Within each neuron and each branch order, we quantified the number of potentiated spines, n_i, and the total number of spines, α_i, in each dendritic segment i. We also calculated the total number of potentiated spines, N, and all spines, A, at the corresponding branch order. If potentiated spines were allocated randomly, one would expect $n_i/N \approx \alpha_i/A$. We performed a stochastic simulation to estimate the distribution of expected $\hat{n}_i$, $P(\hat{n}_i)$, under the random allocation hypothesis for each segment and compared with our data. Compared with the simulated random allocation, the data contained an excess of segments with zero potentiated spines, and an excess of segments with more-than-expected potentiated spines (Fig. 4c). These findings point to the presence of 'silent' segments (with respect to plasticity), as well as a dendrite-level clustering of plasticity.

Finally, we examined whether potentiated spines showed fine-scale clustering within individual dendritic segments. For each neuron, we calculated the interspine contour distance between all pairs of spines. The pairwise distance distribution between potentiated spines showed a decay with a length constant of 8.0 μm (95% confidence interval, 6.5 to 10). In a simulation where we took the same number of potentiated spines and distributed them randomly and independently among all spines, the corresponding distribution for randomly selected spines was flat (Fig. 4d and Extended Data Fig. 9a). We then quantified the distribution of cluster size, that is, the number of potentiated spines within each cluster (Fig. 4e, Extended Data Fig. 9b and Supplementary Information). In CFC-treated mice, potentiated spines were more likely to be in clusters of ≥2 spines compared with the simulated random allocation (potentiated: 57 ± 4.3% of spines were in clusters, mean ± s.e.m.; randomly allocated: 7.2 ± 1.5% clustered; $P = 2.0 \times 10^{-4}$ by Wilcoxon signed-rank test). Clustering of potentiated spines was similar in context-only control mice (context-only: 62 ± 5.0%, mean ± s.e.m.; $P = 0.20$ by two-sided Wilcoxon rank-sum test; Fig. 4e and Extended Data Fig. 9b). These analyses illustrate how pulse-chase HT labeling can map subcellular details of synaptic potentiation.

Discussion

We developed EPSILON, a method to map AMPAR exocytosis with single-synapse resolution during defined time windows in vitro and in vivo. Pulse-chase HaloTag labeling with membrane-impermeable dyes tags AMPAR exocytosis across large brain regions and in deep brain structures. We validated EPSILON in cultured neurons and demonstrated that AMPAR exocytosis is a robust proxy for synaptic potentiation. During fear conditioning experiments in mice, AMPAR exocytosis correlated tightly with cFos expression on a cell-by-cell basis in CA1 pyramidal neurons. We observed preferential plasticity in the perisomatic region in these cells, and clustered plasticity at the level of branches and sub-branch regions. These experiments connected synapse-level plasticity to cell-level engram formation.

A longstanding question in the engram field has been to identify the biophysical mechanisms by which cFos-positive engram cells modulate circuit dynamics to encode a memory[25]. Our work shows that cFos expression can serve as a surrogate for total synaptic plasticity. This finding connects the seemingly disparate bodies of work on engram cells and on synaptic encoding of memories. Mice exposed to the same context without aversive stimulus exhibited less AMPAR exocytosis and lower cFos expression. We did not observe a correlation between AMPAR exocytosis and cFos expression in these mice, but this may be a consequence of the low overall cFos expression: there might be a correlation in the subpopulation of neurons with high cFos expression (Fig. 3m), but these neurons were too rare for us to analyze. The differences between the CFC versus context-only measurements suggest an important role for reinforcement signals in mediating both AMPAR exocytosis and cFos expression.

Building on these observations, we examined the subcellular distributions of synaptic plasticity in engram neurons. Dendrites of CA1 pyramidal neurons receive synaptic inputs from multiple pathways arranged in a laminar distribution. It has been proposed that distal input onto apical dendrites from entorhinal cortex acts as an instructive signal, which modulates plasticity that primarily occurs at the proximal inputs from CA3 (ref. 28). Our results are consistent with this picture and further show that under our experimental paradigms there was little potentiation of the distal inputs. Choi et al. showed that in CFC-treated mice, synapses between CA3 engram cells and CA1 engram cells were enlarged relative to nonengram neurons[7], but it was not clear whether this enlargement preceded the CFC treatment or was a consequence of the treatment. We also observed that the distribution of potentiated spines approximately matched the previously reported distribution of CA3 inputs[29], consistent with the observations of Choi et al. Our work further showed that the increase in AMPAR density occurred after the CFC treatment, implying that the CFC treatment induced the synaptic plasticity.

We also observed clustering of synaptic plasticity at the segment level, aligning with previous theoretical predictions and in vivo observations[30]. This finding supports the possibility that individual dendrites can serve as units for memory allocation. This dendritic segment-level plasticity may arise from compartmentalized calcium influx, which can initiate postsynaptic signaling pathways associated with LTP[31]. Finally we observed short-range (<10 µm) clustering of potentiated spines, consistent with previous observations in cultured neurons and in superficial cortex in vivo[5,32]. This clustering may originate either from co-activated synapses[33] or from diffusion of small GTPases between nearby spines[34]. Clustered plasticity has been proposed to facilitate local dendritic spike generation[12].

There are several possible extensions of the EPSILON technique. First, one could use three or more dyes to map AMPAR exocytosis patterns over two or more epochs (for example, during distinct memory encodings). This approach could highlight overlap in synaptic-level memory networks, or reveal temporal correlations in AMPAR exocytosis rates. Second, one could use in vivo real-time imaging (Extended Data Fig. 10a,b) to track independently the synaptic concentrations of AMPARs labeled with Dye 1 and Dye 2 (Fig. 1h and Extended Data Fig. 2d). This would reveal the relative timing and importance of lateral AMPAR recruitment versus exocytosis in synaptic plasticity. For this application, use of a fluorogenic Dye 2 would minimize background from unreacted dye. Third, one could analyze the data to locate spines containing only Dye 2, and not Dye 1, as a marker of new spine formation (Extended Data Fig. 10c). Fourth, one could use a membrane-permeable Dye 2 or Dye 3. This would relate the population of surface AMPARs to the reservoir of intracellular AMPARs.

AMPAR exocytosis is only one of many biological mechanisms involved in synaptic plasticity, and the relative contributions of different mechanisms across cell types and across stages of plasticity are not fully understood. For example, synaptic weight changes can occur through lateral capture of extrasynaptic AMPARs[4], through posttranslational modifications[35] and through changes of subunit stoichiometry[36]. Several experiments have used knockouts of postsynaptic vesicle fusion machinery to block plasticity-related AMPAR exocytosis, but there has been controversy over which types of memory formation require AMPAR exocytosis[37–39]. To address this issue, it will be useful to monitor AMPAR exocytosis and postsynaptic voltage or calcium concurrently during learning tasks.

A further limitation of EPSILON is that under basal conditions, AMPARs turn over in the synapse with a half-life of ~50 h (Fig. 2h,i). EPSILON experiments can reliably probe plasticity-related exocytosis only on shorter timescales. We restricted plasticity-related pulse-chase intervals to <4 h. It is not known whether there are synapses in which elevated AMPAR exocytosis is counterbalanced by elevated endocytosis; such synapses would bind Dye 2 in an EPSILON assay but may not be potentiated. It will be beneficial to develop techniques to monitor AMPAR endocytosis at the same time as exocytosis. For example, labeling with a membrane-impermeable pH-sensitive Dye 1 could reveal internalization of AMPARs into acidic vesicles.

Our decision to express HT-GluA1 rather than knocking HT into the endogenous *Gria1* locus was motivated by earlier reports on SEP-GluA1. Overexpression of SEP-GluA1 in both cultured neurons and in vivo did not perturb the neuron's intrinsic or synaptic properties[5], while SEP-GluA1 knock-in decreased GluA1 messenger RNA and protein expression[40]. Indeed, our control measurements found no significant effects of HT-GluA1 expression on intrinsic excitability (Extended Data Fig. 3h,i), spine density (Extended Data Fig. 3j,k), total AMPAR level (Extended Data Figs. 1e and 3l,m), synaptic AMPAR/NMDAR current ratio (Fig. 2b–e) or uncaging-induced spine growth (Extended Data Fig. 2a,b). Nonetheless, future uses of EPSILON may benefit from insertion of small and readily labeled tags into the endogenous locus via transgenic[40] or CRISPR-based knock-in[9] approaches. A transgenic approach was successfully used to fuse the biotin acceptor peptide to GluA2, although the reliance on multiple exogenously delivered proteins presented an obstacle for in vivo pulse-chase experiments[9].

The EPSILON technique provides complementary information compared with other approaches to monitoring AMPAR dynamics in vivo. In vivo two-photon microscopy of SEP-GluA1 has been used to observe AMPAR insertion at individual synapses during memory formation[5]. However, despite progress in machine learning-based image analysis[41], the requirement for high-resolution imaging in vivo restricts application of SEP-GluA1 to optically accessible brain regions[42]. Further, the requirement for head-fixed, real-time imaging constrains the possible behavioral paradigms[43]. The dual-eGRASP technique maps synaptic connections between defined neuronal populations, including under control of activity-dependent promoters[7]. This technique separates the in vivo recording from the ex vivo measurement and so is applicable to deep brain regions, but does not directly probe the strength or timing of plasticity events. The eGRASP technique also requires targeted expression of distinct components in pre- and postsynaptic neurons, and thus does not capture all synapses in a given postsynaptic cell. The SYNPLA technique maps AMPAR density in synapses of genetically defined neurons, but it also lacks the capability to probe changes in synaptic strength during a defined time window[8]. EPSILON maps AMPAR exocytosis synaptic resolution and within a user-defined time window, and is not constrained by optical access in vivo. EPSILON provides a powerful tool for studying synaptic plasticity and has the potential to be extended to other transmembrane proteins.

Online content

Any methods, additional references, Nature Portfolio reporting summaries, source data, extended data, supplementary information, acknowledgements, peer review information; details of author contributions and competing interests; and statements of data and code availability are available at https://doi.org/10.1038/s41593-025-01922-5.

References

1. Martin, S. J., Grimwood, P. D. & Morris, R. G. Synaptic plasticity and memory: an evaluation of the hypothesis. *Annu. Rev. Neurosci.* **23**, 649–711 (2000).
2. Wu, Q.-L., Gao, Y., Li, J.-T., Ma, W.-Y. & Chen, N.-H. The role of AMPARs composition and trafficking in synaptic plasticity and diseases. *Cell. Mol. Neurobiol.* **42**, 2489–2504 (2022).
3. Patterson, M. A., Szatmari, E. M. & Yasuda, R. AMPA receptors are exocytosed in stimulated spines and adjacent dendrites in a Ras-ERK–dependent manner during long-term potentiation. *Proc. Natl Acad. Sci. USA* **107**, 15951–15956 (2010).
4. Choquet, D. & Opazo, P. The role of AMPAR lateral diffusion in memory. *Semin. Cell Dev. Biol.* **125**, 76–83 (2022).
5. Zhang, Y., Cudmore, R. H., Lin, D.-T., Linden, D. J. & Huganir, R. L. Visualization of NMDA receptor–dependent AMPA receptor synaptic plasticity in vivo. *Nat. Neurosci.* **18**, 402–407 (2015).
6. Kim, J. et al. mGRASP enables mapping mammalian synaptic connectivity with light microscopy. *Nat. Methods* **9**, 96–102 (2012).
7. Choi, J.-H. et al. Interregional synaptic maps among engram cells underlie memory formation. *Science* **360**, 430–435 (2018).
8. Dore, K. et al. SYNPLA, a method to identify synapses displaying plasticity after learning. *Proc. Natl Acad. Sci. USA* **117**, 3214–3219 (2020).
9. Getz, A. M. et al. High-resolution imaging and manipulation of endogenous AMPA receptor surface mobility during synaptic plasticity and learning. *Sci. Adv.* **8**, eabm5298 (2022).
10. Bulovaite, E. et al. A brain atlas of synapse protein lifetime across the mouse lifespan. *Neuron* **110**, 4057–4073 (2022).
11. Mohar, B. et al. DELTA: a method for brain-wide measurement of synaptic protein turnover reveals localized plasticity during learning. *Nat. Neurosci.* https://doi.org/10.1038/s41593-025-01923-4 (2025).
12. Kastellakis, G. & Poirazi, P. Synaptic clustering and memory formation. *Front. Mol. Neurosci.* **12**, 300 (2019).
13. Watson, J. F., Ho, H. & Greger, I. H. Synaptic transmission and plasticity require AMPA receptor anchoring via its N-terminal domain. *eLife* **6**, e23024 (2017).
14. Bensussen, S. et al. A viral toolbox of genetically encoded fluorescent synaptic tags. *iScience* **23**, 101330 (2020).
15. Xie, L. et al. A dynamic interplay of enhancer elements regulates Klf4 expression in naïve pluripotency. *Genes Dev.* **31**, 1795–1808 (2017).
16. Kleinjan, M. S. et al. Dually innervated dendritic spines develop in the absence of excitatory activity and resist plasticity through tonic inhibitory crosstalk. *Neuron* **111**, 362–371 (2023).
17. Wong, V. C. et al. Plasticity-induced actin polymerization in the dendritic shaft regulates intracellular AMPA receptor trafficking. *eLife* **13**, e80622 (2024).
18. Lu, W. et al. Subunit composition of synaptic AMPA receptors revealed by a single-cell genetic approach. *Neuron* **62**, 254–268 (2009).
19. Dörrbaum, A. R., Kochen, L., Langer, J. D. & Schuman, E. M. Local and global influences on protein turnover in neurons and glia. *eLife* **7**, e34202 (2018).
20. Trachtenberg, J. T. et al. Long-term in vivo imaging of experience-dependent synaptic plasticity in adult cortex. *Nature* **420**, 788–794 (2002).
21. Barrientos, S. A. & Tiznado, V. Hippocampal CA1 subregion as a context decoder. *J. Neurosci.* **36**, 6602–6604 (2016).
22. Ramirez, S. et al. Creating a false memory in the hippocampus. *Science* **341**, 387–391 (2013).
23. Josselyn, S. A. & Tonegawa, S. Memory engrams: recalling the past and imagining the future. *Science* **367**, eaaw4325 (2020).
24. Hebb, D. O. *The Organization of Behavior: A Neuropsychological Theory* (Psychology Press, 2005).
25. Han, D. H., Park, P., Choi, D. I., Bliss, T. V. & Kaang, B.-K. The essence of the engram: cellular or synaptic? *Semin. Cell Dev. Biol.* **125**, 122–135 (2022).
26. Curzon, P., Rustay, N. R. & Browman, K. E. in *Methods of Behavior Analysis in Neuroscience* Ch. 2 (CRC/Taylor & Francis, 2009).
27. Park, K. & Chung, C. Systemic cellular activation mapping of an extinction-impaired animal model. *Front. Cell. Neurosci.* **13**, 99 (2019).
28. Magee, J. C. & Grienberger, C. Synaptic plasticity forms and functions. *Annu. Rev. Neurosci.* **43**, 95–117 (2020).
29. Arai, A., Black, J. & Lynch, G. Origins of the variations in long-term potentiation between synapses in the basal versus apical dendrites of hippocampal neurons. *Hippocampus* **4**, 1–9 (1994).
30. Branco, T. & Häusser, M. The single dendritic branch as a fundamental functional unit in the nervous system. *Curr. Opin. Neurobiol.* **20**, 494–502 (2010).
31. Landau, A. T. et al. Dendritic branch structure compartmentalizes voltage-dependent calcium influx in cortical layer 2/3 pyramidal cells. *eLife* **11**, e76993 (2022).
32. Makino, H. & Malinow, R. Compartmentalized versus global synaptic plasticity on dendrites controlled by experience. *Neuron* **72**, 1001–1011 (2011).
33. Bloss, E. B. et al. Single excitatory axons form clustered synapses onto CA1 pyramidal cell dendrites. *Nat. Neurosci.* **21**, 353–363 (2018).
34. Murakoshi, H., Wang, H. & Yasuda, R. Local, persistent activation of Rho GTPases during plasticity of single dendritic spines. *Nature* **472**, 100–104 (2011).
35. Routtenberg, A. & Rekart, J. L. Post-translational protein modification as the substrate for long-lasting memory. *Trends Neurosci.* **28**, 12–19 (2005).
36. Park, P. et al. The role of calcium-permeable AMPARs in long-term potentiation at principal neurons in the rodent hippocampus. *Front. Synaptic Neurosci.* **10**, 42 (2018).
37. Plitt, M. H., Kaganovsky, K., Südhof, T. C. & Giocomo, L. M. Hippocampal place code plasticity in CA1 requires postsynaptic membrane fusion. Preprint at *bioRxiv* https://doi.org/10.1101/2023.11.20.567978 (2023).
38. Shi, S. et al. Syntaxin-3 is dispensable for basal neurotransmission and synaptic plasticity in postsynaptic hippocampal CA1 neurons. *Sci. Rep.* **10**, 709 (2020).
39. Huang, M. et al. Neuronal SNAP-23 is critical for synaptic plasticity and spatial memory independently of NMDA receptor regulation. *iScience* **26**, 106664 (2023).
40. Graves, A. R. et al. Visualizing synaptic plasticity in vivo by large-scale imaging of endogenous AMPA receptors. *eLife* **10**, e66809 (2021).
41. Xu, Y. K. T. et al. Cross-modality supervised image restoration enables nanoscale tracking of synaptic plasticity in living mice. *Nat. Methods* **20**, 935–944 (2023).
42. Wang, C. et al. Multiplexed aberration measurement for deep tissue imaging in vivo. *Nat. Methods* **11**, 1037–1040 (2014).
43. Juczewski, K., Koussa, J. A., Kesner, A. J., Lee, J. O. & Lovinger, D. M. Stress and behavioral correlates in the head-fixed method: stress measurements, habituation dynamics, locomotion, and motor-skill learning in mice. *Sci. Rep.* **10**, 12245 (2020).

Methods

Animals

All experiments were performed on 8–12-week-old male and female C57BL/6 or CD-1 mice purchased from Charles River Laboratories. All animal procedures were in accordance with the US National Institutes of Health *Guide for the Care and Use of Laboratory Animals* and were approved by the Institutional Animal Care and Use Committee at Harvard University.

DNA constructs

Standard methods of molecular cloning were used to create the constructs. The myc-GluA2 plasmid was provided by the Richard Huganir lab at Johns Hopkins University[5]. Plasmids and sequences created for this project are on Addgene or available upon request.

pTL024 (Addgene 192517). Signal sequence-HaloTag-GluA1 (abbreviated HT-GluA1), driven by human synapsin 1 gene (hSynI) promoter.

Plasmid pTL024 was assembled from three fragments: the N-terminal signal sequence, the HaloTag protein and GluA1. The N-terminal signal sequence was amplified from pCI-SEP-GluR1, Addgene 24000. The HaloTag protein was amplified from Voltron, Addgene 119033. GluA1, along with a 15-amino-acid linker, was amplified from CAG::SEP-GluA1, a gift of R. Huganir[5]. The fragments were assembled together with Gibson Assembly[44] and cloned into pLenti hSynI vector (HT075 from ref. 45).

pDK034. TeTX-LC-IRES-eGFP, driven by cytomegalovirus (CMV) promoter.

Plasmid pDK034 was assembled from three fragments: TeTX-LC, IRES sequences and eGFP. TeTX-LC was amplified from pFsynW-TeTx-LC, Addgene 197284. IRES sequences were amplified from FCK_KCC2_IRES_mOrange plasmid (lab stock). eGFP was amplified from CamKII::PSD95.FingR-eGFP-CCR5TC, Addgene 126218. The fragments were assembled together with Gibson Assembly and cloned into pLenti CMV vector (lab stock).

pTL028 (Addgene 192520). Cre-on AAV expression vector of HaloTag fused to the N terminus of GluA1, driven by human synapsin 1 gene (SYN1, usually called hSyn) promoter. The open reading frame of pTL024 was flipped and cloned into a pAAV_hSyn-DIO vector (Addgene 107704).

Synthesis of AF_{647}-HTL

AF_{647} NHS ester (5 mg, 4.0 μmol) and HaloTag amine (O2) ligand (1.3 mg, 6.0 μmol, 1.5 equivalents (eq)) were combined in *N*,*N*-dimethylformamide (1 ml), and *N*,*N*-diisopropylethylamine (3.5 μl, 20.0 μmol, 5 eq) was added. The reaction was stirred at room temperature for 18 h while shielded from light. It was subsequently purified by reverse-phase HPLC (5–30% MeCN/H_2O, linear gradient, with constant 0.1% v/v TFA additive; 20-min run; 42-ml min^{-1} flow; Gemini-NX 5 μm, 30 × 150 mm^2) to provide 3.2 mg (68%) of the title compound as a blue solid. Analytical HPLC: retention time (t_R) = 13.9 min, >99% purity (10–50% MeCN/H_2O, linear gradient, with constant 0.1% v/v TFA additive; 20-min run; 1-ml min^{-1} fl**ow; Eclipse XDB 5 μm, 4.6 × 150 mm^2; detection at 650 nm; electrospray ionization (ESI), positive ion mode); mass spectrometry (ESI) calculated for $C_{46}H_{67}ClN_3O_{15}S_4$ $[M]^+$ 1,064.3, found 1,064.1; mass spectrometry (ESI) calculated for $C_{46}H_{68}ClN_3O_{15}S_4$ $[M+H]^{2+}$ 532.7, found 532.6.

Primary neuron culture

Neuron culture was as previously described[46].

Virus packaging

In-house preparations of lentivirus used a second-generation lentivirus packaging system using HEK293T cells (ATCC, cat. no. CRL-3216), following the protocol previously described[46]. High-titer HT-GluA1 AAV2/9 virus was generated at the Janelia Vector Core.

Lentiviral transduction of cultured neurons

The hSyn::HT-GluA1 vectors were introduced to the neurons via lentiviral transduction at 7 d in vitro (DIV7) or DIV14. The lentiviral vectors were added directly to the neuronal cultures in fresh BPNM/SM1 medium. The neuronal cultures were then incubated with the lentivirus-containing medium for 12 h at 37 °C and 5% CO_2, followed by a medium replacement with lentivirus-free medium. Experiments were conducted after 7 d. Lentiviruses were produced using the same protocol for both CamKII::PSD95.FingR-eGFP-CCR5TC and CMV::TeTX-LC-IRES-eGFP vectors, and the transduction was conducted 3 d after the transduction of hSyn::HT-GluA1.

Manders' overlap coefficients

The Manders' coefficients (M1 and M2) were calculated between two channels (HT-GluA1 and PSD95) for each neuron, as previously described[47], using MATLAB. Briefly, the images in each color channel were binarized with a threshold set by the Otsu algorithm. M1 and M2 were calculated via:

$$M_1 = \mathrm{sum}(B_{\text{HT-GluA1}} \odot I_{\text{HT-GluA1}} \odot B_{\text{PSD95}}) \Big/ \mathrm{sum}(B_{\text{HT-GluA1}} \odot I_{\text{HT-GluA1}})$$

$$M_2 = \mathrm{sum}(B_{\text{PSD95}} \odot I_{\text{PSD95}} \odot B_{\text{HT-GluA1}}) \Big/ \mathrm{sum}(B_{\text{PSD95}} \odot I_{\text{PSD95}})$$

where I denotes the original image, B denotes a binary mask obtained with a threshold set by the Otsu algorithm, $\odot$ is elementwise multiplication.

In vitro labeling kinetics

Cultured neurons expressing HT-GluA1 at DIV14 were incubated with 100 nM AF_{488}-HTL or 1 μM JF_{549i}-HTL or 1 μM AF_{647}-HTL in fresh BPNM/SM1 medium for different time durations (5 s, 30 s, 5 min and 30 min for 100 nM AF_{488}-HTL; 5 s, 10 s, 30 s, 2 min, 5 min and 10 min for 1 μM JF_{549i}-HTL and 1 μM AF_{647}-HTL) at 37 °C and 5% CO_2. The neurons were then washed twice with PBS for 1 min each and fixed with 4% paraformaldehyde. The fixed neuron cultures were then washed in PBS for 24 h. All media were heated to 37 °C before use.

In vitro turnover rate

Cultured neurons expressing HT-GluA1 at DIV14 were incubated with 100 nM AF_{488}-HTL in fresh BPNM/SM1 medium for 5 min at 37 °C and 5% CO_2. The neurons were then washed twice with PBS for 1 min each and the medium was replaced with dye-free medium. To label new surface HT-GluA1, the medium was replaced with 1 μM JF_{549i}-HTL in fresh BPNM/SM1 medium at different time points. After incubating for 5 min at 37 °C and 5% CO_2, neurons were washed twice with PBS for 1 min each and fixed with 4% paraformaldehyde. The fixed neuron cultures were then washed in PBS for 24 h. All media were heated to 37 °C before use.

MNI-glutamate uncaging

MNI-glutamate uncaging was conducted as previously described[16]. Briefly, live-cell imaging of cultured neurons was carried out on an LSM 980 (operated with Zeiss Zen (blue edition)) with a ×63 oil immersion objective at 34 °C. Neurons were incubated with an imaging buffer containing 10 mM HEPES, 130 mM NaCl, 5 mM KCl, 30 mM D-glucose, 2 mM $CaCl_2$, 1 mM $MgCl_2$, supplemented with 1 μM tetrodotoxin (TTX) for 5 min and then stained with 1 μM Dye 1 (AF_{647}-HTL) for 1 min in the same buffer. After neurons were washed three times with the imaging buffer without dye, the buffer was changed to the same one without TTX or Mg^{2+}, and supplemented with 1 μM glycine and 2 mM MNI-glutamate. Z-stack images were acquired in eGFP and Dye 1 channels 1 min before uncaging pulses were delivered. Spines were focally stimulated to a diffraction-limited spot at 405 nm with 60 uncaging pulses delivered at 1 Hz. To monitor spine growth, z-stack images in the eGFP channel were acquired every 3 min starting 1 min after uncaging. Then, 25 min after uncaging, the Mg^{2+}-free buffer was replaced with the standard imaging buffer containing 1 µM Dye 2 (JF_{549i}-HTL), and the neurons were stained for 1 min. After washing the neurons twice, z-stack images were acquired in eGFP, Dye 1 and Dye 2 channels.

Pulse-chase labeling in cultured neurons during cLTP

Cultured neurons expressing HT-GluA1 at DIV21 were washed twice with a stimulation buffer containing 150 mM NaCl, 2 mM $CaCl_2$, 5 mM KCl, 10 mM HEPES, 30 mM D-glucose, 0.5 µM TTX, 20 mM bicuculline and 1 µM strychnine. The neurons were then exposed to 1 µM Dye 1 (AF_{647}-HTL) in the stimulation buffer at 37 °C and 5% CO_2 for 1 min. The neurons were then washed twice with the stimulation buffer and then incubated in the stimulation buffer supplemented with 0.2 mM glycine and 1 µM Dye 2 (JF_{549i}-HTL) for 10 min. The neurons were then washed twice with a washing buffer with the same composition but supplemented with an additional 2 mM $MgCl_2$ and then stained with 1 µM Dye 2 again in the washing buffer for 5 min. The neurons were washed twice with the washing buffer and fixed with 4% paraformaldehyde. The fixed neuron cultures were washed in PBS for 24 h. TeTx-LC coexpressing neurons underwent the same experimental conditions. The negative control cultures were exposed to the stimulation buffer without glycine. All media were pre-incubated with 5% CO_2 for 30 min and heated to 37 °C before use.

GluA1 immunohistochemistry in cultured neurons

After the neurons were fixed and washed as described above, the fixed neurons were permeabilized with PBST1 (0.1% Triton-X in PBS) for 10 min at room temperature on a shaker. The neurons were then blocked with 1% BSA in PBST2 (0.1% Tween 20 in PBS) for 30 min on a shaker. The neurons were incubated with a mouse anti-GluA1-CTD (C-terminal domain) primary antibody (1:500 dilution in 1% BSA in PBST2; Synaptic Systems, cat. no. 182 011) for 1 h at room temperature on a shaker. Neurons were then washed in PBST2 for 5 min (×3), followed by 1 h of incubation with secondary antibody (1:500 in 1% BSA in PBST2; AF_{647} goat anti-mouse; Abcam, cat. no. A-150115) at room temperature. After two additional 5-min washes and one 24-h wash in PBS at room temperature, the neurons were imaged on a confocal microscope.

IUE

Progenitor cells in layer 2/3 of the embryonic mouse brain were transfected using IUE. Pregnant CD-1 mice were used and DNA solution containing Fast Green was injected into the lateral ventricle of each embryo through a pulled-glass pipette. Electric pulses were applied using 5-mm Pt electrodes. The angle of electrodes was adjusted to target the specified brain region (barrel cortex or hippocampal CA1). The electroporation protocol comprised five pulses of 35 V, with a frequency of 1 Hz and a duration of 50 ms. The DNA solution used contained HT-GluA1, myc-GluA2 at a ratio of 1:1 (final concentration: 2 µg μl^{-1} each). For the coexpression with GPI-eGFP or PSD95.FingR-eGFP, the DNA solution contained HT-GluA1, myc-GluA2 and GPI-eGFP or PSD95.FingR-eGFP at a ratio of 2:2:1 (final concentration: 2 µg μl^{-1} for HT-GluA1 and myc-GluA2; 1 µg μl^{-1} for GPI-GFP or PSD95.FingR-eGFP).

Patch-clamp electrophysiology

Coronal brain slices (300 µm) were prepared from CD-1 mice of either sex between postnatal days 14 and 16. IUE was used for HT-GluA1 expression in cortical layer 2/3 neurons. Standard whole-cell recording was performed at 34 °C during a continuous perfusion at 2 ml min^{-1}. The perfusion buffer contained 124 mM NaCl, 3 mM KCl, 26 mM $NaHCO_3$, 1.25 mM NaH_2PO_4, 2 mM $MgCl_2$, 15 mM D-glucose and 2 mM $CaCl_2$ (saturated with 95% O_2 and 5% CO_2). Cortical layer 2/3 neurons were visualized using a custom-built upright microscope. The whole-cell internal solution contained 8 mM NaCl, 130 mM $KMeSO_3$, 10 mM HEPES, 5 mM KCl, 0.5 mM EGTA, 4 mM Mg-ATP, 0.3 mM Na_3-GTP. The pH was adjusted to 7.2–7.3 with KOH and osmolarity was set to 290–295 mOsm l^{-1}. Borosilicate glass pipettes were used with a resistance of 3–5 MΩ (WPI, cat. no. 1B150F-4). Patch-clamp recordings were acquired and filtered at 10 kHz with the internal Bessel filter using a Multiclamp 700B (Molecular Devices) and digitized with PCIe-6323 (National Instruments) at 100 kHz. Following the whole-cell configuration, membrane capacitance (C_m) and membrane resistance (R_m) were estimated under voltage-clamp mode. Resting membrane potential, rheobase and spike rates were measured under current-clamp mode. Rheobase was defined as the minimum current step (in 500-ms duration) required to trigger at least one spike. Whole-cell recordings were monitored and analyzed in MATLAB.

To measure evoked EPSCs, voltage-clamp experiments were performed with a stimulating electrode (FHC, cat. no. CBAPB50) placed 100–200 µm laterally to activate layer 2/3 inputs. Holding potential was −70 mV. The whole-cell internal solution contained (in mM): 8 NaCl, 130 $CsMeSO_3$, 10 HEPES, 0.5 EGTA, 4 Mg-ATP, 0.3 Na_3-GTP, 5 QX-314, 0.1 spermine. The pH was adjusted to 7.2–7.3 with CsOH and osmolarity was set to 290–295 mOsm l^{-1}. The perfusion buffer contained 50 µM picrotoxin (Thermo Scientific) and 10 µM (+)-bicuculline (Enzo Life Sciences) to prevent $GABA_A$ receptor-mediated transmission. After a stable baseline of at least 5 min, the input–output relationships were estimated by varying the stimulus intensity from 3 to 15 V in 3-V increments (0.1-ms duration). Stimulation frequency was 0.1 Hz. For measuring the AMPAR/NMDAR ratio, cells were clamped at a holding potential of −70 mV to measure the peak of AMPAR-mediated synaptic transmission. NMDAR-mediated currents were estimated at 75 ms after the stimulus onset at a holding potential of +40 mV. Example traces were an average of five consecutive responses, collected from typical experiments (stimulus artifacts were blanked for clarity). Experiments were accepted for analysis if series resistance values were <20 MΩ and varied by <15% throughout the experiment.

Cranial window surgery and stereotaxic intracranial AAV injection

CD-1 mice aged 8–10 weeks were given a ketamine/dexmedetomidine (77 mg kg^{-1} and 0.33 mg kg^{-1}, respectively) solution for anesthesia and were positioned in a stereotaxic apparatus. A craniotomy of approximately 3 mm was created on the left barrel cortex of the exposed skull (3.3–3.4 mm lateral, 1.6 mm posterior of bregma) with a dental drill. The HT-GluA1 and CamKII-Cre AAV2/9 viruses were diluted to a final titer of 1×10^{13} and 1×10^{11} genome copies per ml, respectively. The diluted virus was injected at five sites across the craniotomy (80 and 160 µm beneath the dura; 40–60 nl at each depth; 30–60 nl min^{-1}). Following the virus injection, a glass window was placed over the craniotomy and fixed to the skull using silicone gel (KWIK-CAST silicone sealant, WPI). Then, a titanium headplate was attached to the exposed skull using dental cement (C&B Metabond, Parkell, cat. no. 242-3200). After the mice recovered from anesthesia, they were returned to their home cages, and carprofen (5 mg kg^{-1}) and buprenorphine (0.1 mg kg^{-1}) were administered on postsurgery days 0, 1 and 2. The designs of the cranial window and the titanium headplate used in this experiment were based on previously published protocols[45,48].

Intracortical dye injection for two-photon imaging

At 1 week after the cranial window surgery, the mice were brought back to the surgical stage and put under <2% isoflurane anesthesia. The anesthesia was maintained at 1% isoflurane throughout the surgery. The window was removed carefully along with the silicone gel, and the dura was carefully removed based on previously published protocols[48]. Then, 1 µM AF_{488}-HTL was injected at three different sites across the craniotomy, with a rate of 100 nl min^{-1} (80 nl at each depth, with 0.1-mm increments from 0.5 mm to 0 mm beneath the cortical surface).

After dye injection, a new window was placed over the craniotomy and attached to the skull with silicone gel. The animals were then moved to the in vivo imaging setup, and the two-photon imaging session was started 20 min after the dye injection had ended.

In vivo two-photon imaging

Live images were obtained from mice that had undergone cranial window surgery and intracortical dye injection while under anesthesia with isoflurane (1% vol isoflurane/vol O_2) using a custom two-photon laser-scanning microscope controlled by custom LabView code described previously[49]. Throughout the imaging session, the animal was kept anesthetized with a dose of 1–1.5% isoflurane, adjusted to maintain a stable breathing rate. The mouse was kept warm using a heating pad (WPI, cat. no. ATC2000) to maintain a stable body temperature of 37 °C, and ophthalmic eye ointment was applied to both eyes to keep them moist. HT-GluA1 stained with AF_{488}-HTL was excited at 910 nm using a Ti:sapphire laser (Coherent) beam delivered to the back-aperture of the objective. AF_{488} fluorescence was filtered by a band-pass emission filter (Unice, cat. no. FF-3-525/50-25) and delivered onto a photomultiplier tube (Hamamatsu). Image stacks were acquired with a voxel size of 0.18 μm in x and y and a dwell time of 200 μs. The z-step was 1 μm. Images shown in figures were Gaussian filtered to remove speckle noise. The imaging session lasted <1 h.

Installation of dye injection port

Male or female CD-1 mice expressing HT-GluA1 via IUE were selected at age 9–11 weeks and anesthetized using a ketamine/dexmedetomidine solution. To maintain body temperature at 36–37 °C, a heating pad (WPI, cat. no. ATC2000) was placed under the mouse, and ophthalmic eye ointment was applied to the mouse's eyes to keep them moist. Surgical coordinates were identified as indicated in Extended Data Fig. 4a,b, and a hollow titanium ring with an outer diameter of 5 mm, an inner diameter of 2.1 mm and a thickness of 0.35 mm was attached to the skull surrounding the target coordinates with dental cement (C&B Metabond, Parkell, cat. no. 242-3200). Holes were drilled through the skull until only a very thin layer of the skull (~20 μm) remained and the titanium ring was filled with silicone gel which was removed before dye injection and refilled after injection. The mice were returned to their home cages after recovering from anesthesia.

In vivo turnover rate measurement

At 1 week after installation of the injection port at the barrel cortex, mice (age 10–12 weeks) were anesthetized with isoflurane and placed on a surgical platform. At every indicated injection point in Extended Data Fig. 4a, 80 nl of AF_{647}-HTL (1 μM) was injected at a rate of 100 nl min^{-1}. Then, 80 nl of JF_{549i}-HTL (10 μM) was injected at the same points 20 min after the AF_{647}-HTL injection, also at the same rate. After 20 min from the end of the dye injection, the mice were returned to their home cages. Later, at different time points, the mice underwent the second JF_{549i}-HTL injection. At the same injection points as previously described, 80 nl of JF_{549i}-HTL (10 μM) was injected at the same rate. After 20 min from the end of the dye injection, the mice were euthanized and prepared for brain slicing.

Acute whisker stimulation with pulse-chase labeling

Whisker stimulation sessions were conducted 1 week after injection port installation. On the day of stimulation, 2.7 mg kg^{-1} of chlorprothixene hydrochloride dissolved in PBS was intraperitoneally injected before anesthetic induction. Mice (10–12 weeks) were anesthetized with isoflurane on the surgical platform and injected at each point shown in Extended Data Fig. 4a with JF_{549i}-HTL (80 nl, 1 μM) at a rate of 100 nl min^{-1}. After 20 min, AF_{488}-HTL (80 nl, 10 μM) was injected at the same points. After another 20 min from the end of dye injection, the contralateral whiskers were trimmed in a chessboard pattern[20,50,51]. Spared whiskers were deflected at 10 Hz for 180 min with a rotary whisker stimulator. Mice in the control group were placed under the same experimental conditions, but all contralateral whiskers were trimmed. During whisker stimulation, isoflurane level was kept at ~0.5% to maintain shallow anesthesia. After whisker stimulation, the mice underwent the second injection of AF_{488}-HTL (80 nl, 10 μM) as previously described. After 20 min from the end of the dye injection, the mice were euthanized and prepared for brain slicing.

Slice preparation for confocal imaging

Mice were overdosed with isoflurane until their breathing ceased. Their brains were then promptly extracted. The brains were sliced into 300-μm coronal sections using a vibratome (Leica, cat. no. VT1200S) and then fixed in 4% paraformaldehyde for 24 h at 4 °C. The fixed slices were additionally washed in PBS for 48 h on a shaker at room temperature. The slices were mounted (VECTASHIELD PLUS Antifade Mounting Medium, Vectorlabs, cat. no. H-1900-10) to be imaged on confocal imaging systems.

CFC with pulse-chase labeling

In the 5 d before CFC treatment, each mouse was housed alone and habituated to the investigator and anesthesia chamber without isoflurane. On the day of conditioning, the mouse (age 10–12 weeks) was anesthetized for 3 h with 1.0% isoflurane on the surgical platform and injected with AF_{647}-HTL (80 nl, 1 μM) at a rate of 100 nl min^{-1} at every injection point shown in Extended Data Fig. 4b. After 20 min, JF_{549i}-HTL (80 nl, 10 μM) was injected at the same points. The mouse was then returned to its home cage to recover from anesthesia. After 20 min, the mouse underwent conditioning sessions that lasted 300 s. For the first 150 s, the mouse was allowed to explore the conditioning chamber freely. Starting at 150 s and repeating every 30 s for a total of five shocks, the mouse was given 0.7-mA foot shocks of 2-s duration. Mice in the context-only group were placed in the same chamber for 300 s without any shocks. Mice in the home cage control group remained in their home cage. After 90 min from the end of the conditioning session, the mouse was anesthetized with isoflurane on the surgical platform for the second JF_{549i}-HTL injection. Then, 80 nl of JF_{549i}-HTL (10 μM) was injected into the injection points at the same points and rate as previously described. After 20 min from the end of the dye injection, the mouse was euthanized and prepared for brain slicing.

For the experiments in Extended Data Fig. 5a, the same conditioning sessions (with and without shocks) were conducted, except the dye injection steps were skipped. At 1 d after conditioning, mice were exposed to the same context and their freezing (absence of movement except for respiration[26]) levels were measured via video analysis of the first 180 s from re-exposure. Animal motion was tracked using MATLAB code. Briefly, the center of mass of the mouse was tracked for every frame using the regionprops function. Then, the mouse's speed was calculated between each frame, and the time duration during which the speed was slower than 0.03 m s^{-1} was counted as freezing time, taking into account the movement of the center of mass during breathing and system vibrations.

Immunohistochemistry for fixed brain tissue

After the brain was sliced, fixed and washed as described above (slice thickness = 150 μm), the fixed slices were permeabilized with PBST (1% Triton-X in PBS) for 24 h at room temperature on a shaker. The slices were then blocked with 5% BSA in PBST for 1 h on a shaker. For cFos immunostaining, the slices were incubated with a rat anti-cFos primary antibody (1:1,000 dilution in 1% BSA in PBST, Synaptic Systems, cat. no. 226 017) for 24 h at room temperature on a shaker. Slices were then washed in PBST for 20 min (×3), followed by 2-h incubation with secondary antibody (1:500 in 1% BSA in PBST; AF_{488} anti-rat, Invitrogen, cat. no. A-11006) at room temperature. After two additional 20-min washes and one 24-h wash in PBST at room temperature, the mounted slices were imaged on a confocal microscope. For GluA1-CTD immunostaining, the same experimental conditions were used, except different antibodies and their respective dilution factors were used (primary antibody: 1:500 diluted mouse anti-GluA1-CTD, Synaptic Systems, cat. no. 182 011; secondary antibody: 1:500 diluted AF_{647} goat anti-mouse, Abcam, cat. no. 150115). For GFAP immunostaining, the following antibodies were used; primary antibody: 1:500 diluted rabbit anti-GFAP, Abcam, cat. no. 7260; secondary antibody: 1:500 diluted AF_{488} goat anti-rabbit, Invitrogen, cat. no. A11008.

Confocal imaging of HT-GluA1 expressed in cultured rat hippocampal neuron

Confocal images of fixed neuron cultures were acquired using LSM 980 (operated with Zeiss Zen (blue edition)) with a ×20 water immersion objective. AF_{488}, JF_{549i} and AF_{647} were excited with 488-nm, 561-nm and 633-nm lasers, respectively. Pixel size was 0.052 µm by 0.052 µm and the size of each region of interest was 424.27 µm by 424.27 µm (8,192 pixels by 8,192 pixels). Pixel time was 0.51 µs. The same imaging conditions were used throughout all experiments.

Confocal imaging of HT-GluA1 expressed in brain slice

Confocal images of fixed brain slices were acquired using LSM 980 (operated with Zeiss Zen (blue edition)) with a ×20 water immersion objective in z-stack. Images in Figs. 2a (right), 3a (right) and 3d were acquired with a ×63 oil immersion objective. DAPI, eGFP, AF_{488}, JF_{549}, JF_{549i} and AF_{647} were excited with 405-nm, 488-nm, 488-nm, 561-nm, 561-nm and 633-nm lasers, respectively. Nonspecific autofluorescent artifacts were excited with 488 nm for Fig. 2 and 561 nm for Fig. 3 and the detection ranges were from 500 nm to 553 nm for Fig. 2f–i, from 651 nm to 695 nm for Fig. 2j–n and from 500 nm to 553 nm for Fig. 3. Voxel sizes were 0.052 µm by 0.052 µm by 2 µm for Fig. 2 (except for Fig. 2a (right)) and 0.052 µm by 0.052 µm by 1 µm for Fig. 3 (except for Fig. 3a (right)). For Figs. 2a (right) and 3a (right), the voxel size was 0.016 µm by 0.016 µm by 0.23 µm. Pixel time was 0.51 µs for all experiments. The same imaging conditions were used for all samples within each set of experiments.

Image processing and data analysis

See Supplementary Information.

Statistics and reproducibility

All statistical tests performed are specified in the figure legends. Differences with values of $P < 0.05$ were considered statistically significant. Sample sizes were determined by the technical requirements of the experiments. No data were excluded from the analyses. Individual animals were indistinguishable in terms of HT-GluA1 expression status at the time of the experiments and were therefore randomly selected. Data collection was not conducted blinded to experimental conditions.

Statistical analyses were performed using MATLAB. Normality of datasets was assessed with the Shapiro–Wilk test ($P > 0.05$ indicates normal distribution). For paired datasets, a two-tailed paired *t*-test was used for normally distributed data, and a Wilcoxon signed-rank test was used for non-normally distributed data. For unpaired datasets, a two-tailed unpaired *t*-test was used for normally distributed data, and a Mann–Whitney *U*-test was used for non-normally distributed data.

Reporting summary

Further information on research design is available in the Nature Portfolio Reporting Summary linked to this article.

Data availability

All data, including images of dye-stained HT-GluA1-expressing neurons and patch-clamp recordings, are available from the corresponding author upon request.

Code availability

Computer codes for data analysis are available from the corresponding author upon request.

References

44. Gibson, D. G. et al. Enzymatic assembly of DNA molecules up to several hundred kilobases. *Nat. Methods* **6**, 343–345 (2009).
45. Tian, H. et al. Video-based pooled screening yields improved far-red genetically encoded voltage indicators. *Nat. Methods* **20**, 1082–1094 (2023).
46. Lin, D. et al. Time-tagged ticker tapes for intracellular recordings. *Nat. Biotechnol.* **41**, 631–639 (2023).
47. Manders, E., Verbeek, F. & Aten, J. Measurement of co-localization of objects in dual-colour confocal images. *J. Microsc.* **169**, 375–382 (1993).
48. Goldey, G. J. et al. Removable cranial windows for long-term imaging in awake mice. *Nat. Protoc.* **9**, 2515–2538 (2014).
49. Adam, Y. et al. Voltage imaging and optogenetics reveal behaviour-dependent changes in hippocampal dynamics. *Nature* **569**, 413–417 (2019).
50. Holtmaat, A., Wilbrecht, L., Knott, G. W., Welker, E. & Svoboda, K. Experience-dependent and cell-type-specific spine growth in the neocortex. *Nature* **441**, 979–983 (2006).
51. Seaton, G. et al. Dual-component structural plasticity mediated by αCaMKII autophosphorylation on basal dendrites of cortical layer 2/3 neurones. *J. Neurosci.* **40**, 2228–2245 (2020).

Acknowledgements

We thank A. Preecha and S. Begum for technical assistance. We thank R. Huganir for sharing plasmids. We thank M. Tadross, R. Yasuda, S. Grant, B. Mohar, N. Spruston, K. Svoboda and B. Sabatini for helpful discussions. This work was supported by grants from Schmidt Futures and the Gordon and Betty Moore Foundation and by NIH grant no. 1-R21-EY033669. J.D.W.-C. is a Merck Awardee of the Life Sciences Research Foundation. J.B.G. and L.D.L. are supported by the Howard Hughes Medical Institute. The funders had no role in study design, data collection and analysis, decision to publish or preparation of the paper.

Author contributions

A.E.C. and D.K. conceived the project and designed the experiments. D.K. conducted the experiments and analyzed the data. P.P. performed acute brain slice patch-clamp measurements. X.L. contributed to molecular cloning. J.D.W.-C., H.T. and E.M.M. provided advice and technical support. L.D.L. and J.B.G. synthesized and provided the dyes used in this study. D.K. and A.E.C. wrote the paper with input from all authors. A.E.C. supervised the project.

Competing interests

The authors declare no competing interests.

Additional information

Extended data is available for this paper at https://doi.org/10.1038/s41593-025-01922-5.

Supplementary information The online version contains supplementary material available at https://doi.org/10.1038/s41593-025-01922-5.

Correspondence and requests for materials should be addressed to Adam E. Cohen.

Peer review information *Nature Neuroscience* thanks the anonymous reviewers for their contribution to the peer review of this work.

Reprints and permissions information is available at www.nature.com/reprints.

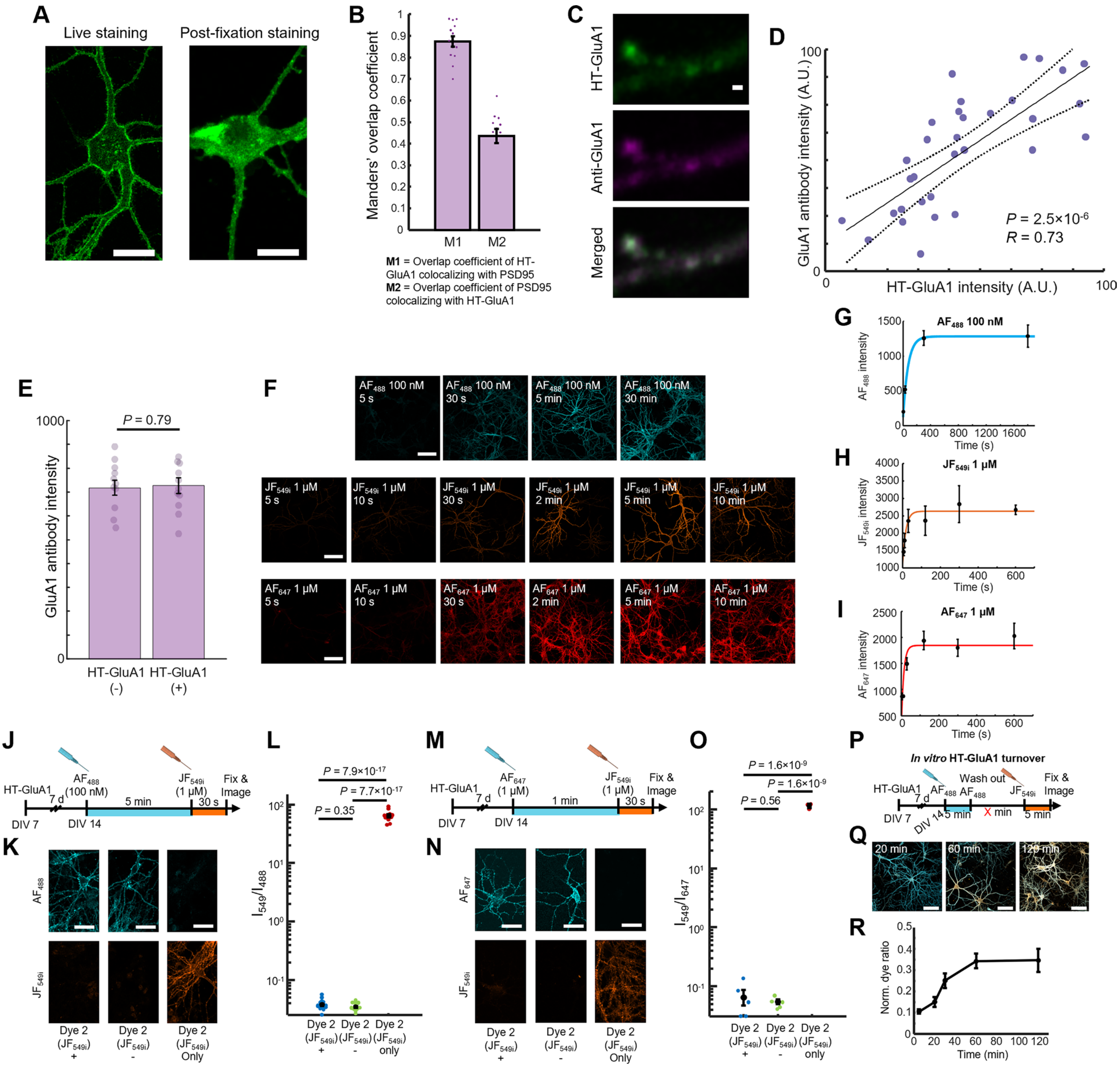

Extended Data Fig. 1 | See next page for caption.

Extended Data Fig. 1 | *In vitro* characterization of EPSILON. (a) Selective labeling of surface HT-GluA1 with membrane-impermeable HTL dye. Left: Cultured neuron expressing HT-GluA1 stained with membrane-impermeable AF_{488}-HTL while alive. Right: Another HT-GluA1 expressing cultured neuron stained with the same dye after fixation to permeabilize the cell membrane. Scale bars 10 µm. **(b)** Manders' overlap coefficient between HT-GluA1 and PSD95 (PSD95.FingR-eGFP). *n* = 13 dendritic segments from 7 neurons. Error bars show mean ± s.e.m. **(c)** Confocal images of a fixed cultured neuron expressing (top) JF_{549}-labeled HT-GluA1 stained with (middle) anti-GluA1-CTD (c-terminal domain) antibody. (Bottom) Merge. Scale bar, 1 µm. **(d)** Relationship between HT-GluA1 intensity and GluA1 antibody intensity among spines. *n* = 32 spines from 5 neurons. *R*, Pearson's linear correlation coefficient, *P* value from two-sided Student's t-test. **(e)** GluA1 expression level in HT-GluA1 +/− neurons stained with anti-GluA1-CTD antibody (*n* = 11 dendritic segments from 5 neurons for each group). Two-sided Wilcoxon rank-sum test. Error bars show mean ± s.e.m. **(f)** Confocal images of fixed cultured neurons showing labeling of HT-GluA1 with AF_{488}-HTL (100 nM, cyan) or JF_{549i}-HTL (1 µM, orange) or AF_{647}-HTL (1 µM, red) at different times after dye addition. Scale bars: 100 µm. **(g-i)** Fluorescence vs. dye incubation time for cultured neurons expressing HT-GluA1 and treated with **(g)** AF_{488}-HTL (100 nM) or **(h)** JF_{549i}-HTL (1 µM) or **(i)** AF_{647}-HTL (1 µM). (*n* = 5 cells for each timepoint). Data are represented as mean ± SD. Red: fitted curve. **(j)** Surface GluA1 was saturated by labeling with 100 nM AF_{488}-HTL for 5 minutes, followed immediately by chase-dye labeling (1 µM of JF_{549i}-HTL for 30 s). **(k)** Confocal images of fixed cultured neurons after saturation with AF_{488}-HTL (left) with and (middle) without JF_{549i}-HTL chase. (Right) JF_{549i}-HTL only without AF_{488}-HTL. Scale bars: 50 µm. **(l)** JF_{549i}-to-AF_{488} intensity ratios (*n* = 16 cells from 3 cultures for Dye 2 +; *n* = 16 cells from 3 cultures for Dye 2 -; *n* = 12 cells from 3 cultures for Dye 2 only). Error bars show mean ± s.e.m. Two-sided Student's t-test. **(m)** Surface GluA1 was saturated by labeling with 1 µM AF_{647}-HTL for 1 minute, followed immediately by chase-dye labeling (1 µM of JF_{549i}-HTL for 30 s). **(n)** Confocal images of fixed cultured neurons (left) with and (middle) without JF_{549i}-HTL after saturation with AF_{647}-HTL. (Right) JF_{549i}-HTL only without AF_{647}-HTL. Scale bars: 50 µm. **(o)** JF_{549i}-to-AF_{647} intensity ratios (*n* = 5 cells from 2 cultures for each group). Error bars show mean ± s.e.m. Two-sided Student's t-test. **(p)** Experimental timeline of surface HT-GluA1 turnover measurement with multi-color labeling. **(q)** Confocal images of fixed cultured neurons showing replacement of old (AF_{488}, cyan) with new (JF_{549i}, orange) AMPARs. Scale bars: 200 µm. Turnover occurred faster in soma and perisomatic neurites than in distal neurites. **(r)** Normalized dye intensity ratio at 5, 20, 30, 60, and 120-min (*n* = 5 cells for each timepoint). Normalized dye intensity ratio: 2nd dye intensity / (1st dye intensity + 2nd dye intensity). Data are represented as mean ± SD. Schematics in **j**, **m** and **p** created using BioRender.com.

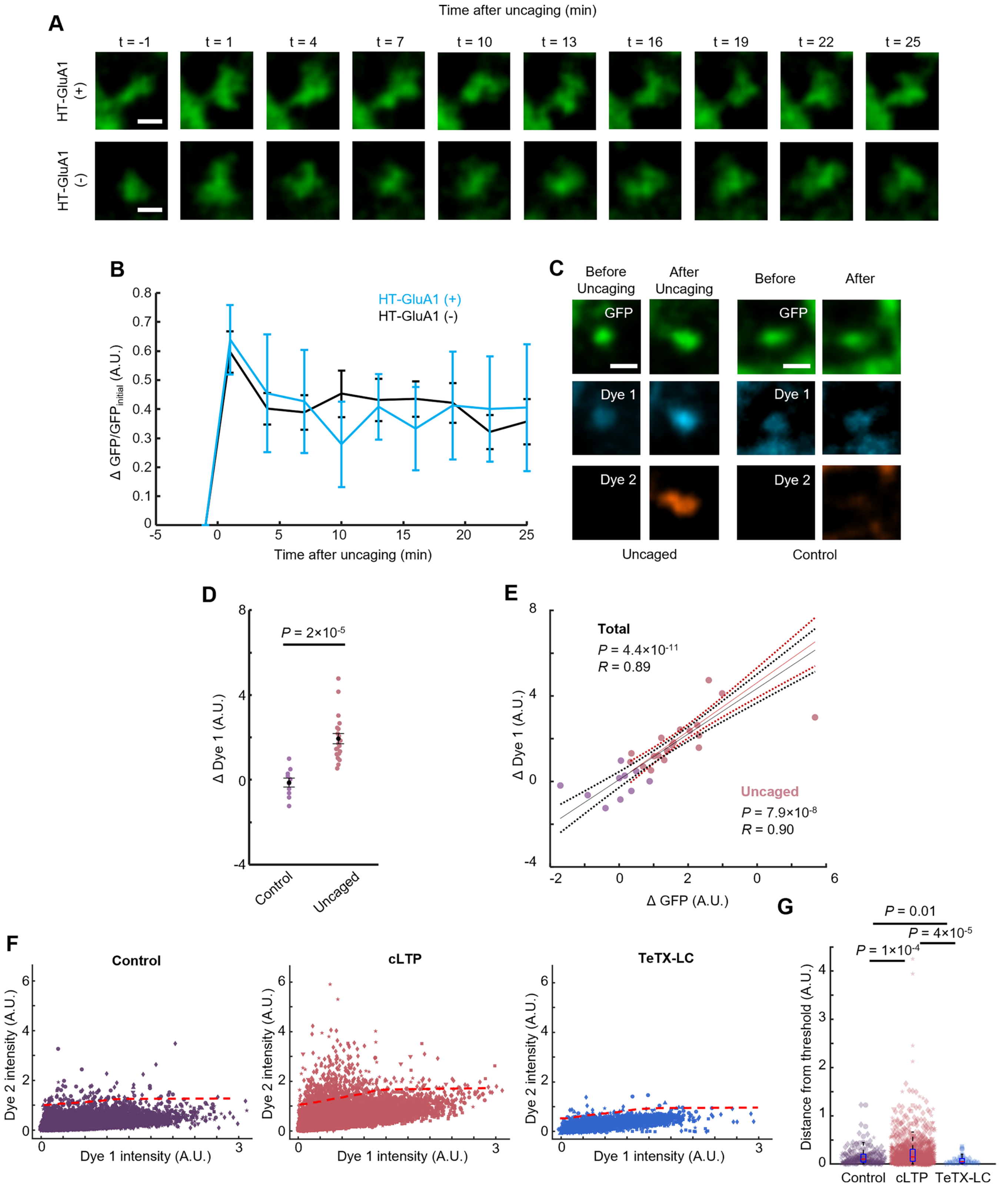

Extended Data Fig. 2 | See next page for caption.

Extended Data Fig. 2 | Effects of MNI-glutamate uncaging and cLTP on AMPAR exocytosis. **(a)** Time-lapse images of the stimulated spines expressing GPI-eGFP +/− HT-GluA1 expression. Scale bars, 10 µm. **(b)** Time course for spine size increases +/− HT-GluA1 expression (HT-GluA1 (+): *n* = 13 spines from 3 neurons; HT-GluA1 (−): *n* = 14 spines from 3 neurons). Error bars show mean ± s.e.m. **(c)** Confocal images of spines expressing GPI-eGFP (green) and HT-GluA1 labeled with Dye 1 (cyan, AF_{647}) and Dye 2 (orange, JF_{549i}), before and after glutamate photo-uncaging. Controls had no glutamate uncaging. Scale bars, 1 µm. **(d)** Dye 1 intensity change for control and uncaged spine groups. Control: *n* = 10 spines; Uncaged: *n* = 20 spines. Two-sided Wilcoxon rank-sum test. Error bars show mean ± s.e.m. **(e)** Correlation between the change in Dye 1 intensity and the change in spine size for spines from (**d**). *R*, Pearson's linear correlation coefficient, *P* value from two-sided Student's t-test. **(f)** Scatterplots of spine fluorescence intensities in the two color channels for (left) control, (middle) cTLP-treated, and (right) TeTX-LC co-expressing neurons. Same data as in Fig. 1m, with vertical scale adjusted to include all spines. Control: *n* = 32,828 spines from 6 cultures; cLTP: *n* = 47,090 spines from 6 cultures; TeTX-LC: *n* = 17,231 spines from 6 cultures. Dye 2 intensity thresholds indicated with dashed lines (see Methods for calculation of threshold). Replicate dishes represented by different shape symbols. **(g)** The extent of AMPAR exocytosis in each spine measured by the fluorescence of Dye 2 above threshold. Spines with Dye 2 intensity higher than the threshold were included for analysis (control: 1,563 ± 112 counts, mean ± s.e.m., *n* = 195 spines, 54 neurons, 6 cultures, cLTP: 2,398 ± 74.9 counts, mean ± s.e.m., *n* = 1,024 spines, 44 neurons, 6 cultures; TeTX-LC: 868.7 ± 147 counts, mean ± s.e.m., *n* = 35 spines, 45 neurons, 6 cultures). Replicate dishes represented by different symbols. Box plot shows extrema, 25th and 75th percentiles and median. Two-sided Wilcoxon rank-sum test.

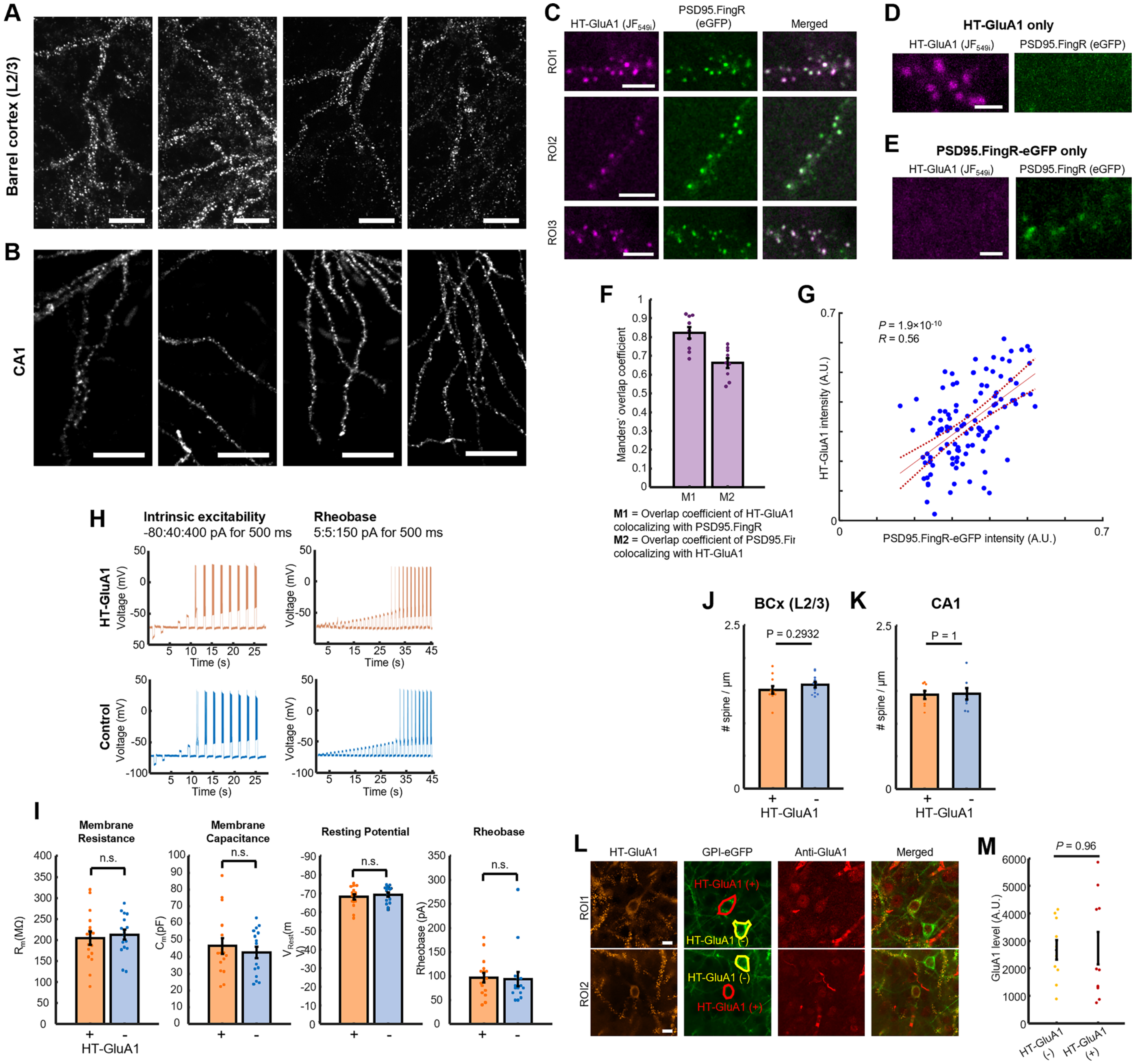

Extended Data Fig. 3 | Validation of EPSILON in mouse brain. HT-GluA1 stained with AF_{647}-HTL in **(a)** barrel cortex **(b)** CA1 pyramidal cells. Each set of micrographs represents a single experiment. Scale bars 50 µm. **(c)** Postsynaptic trafficking of HT-GluA1 in layer 2/3 pyramidal neurons in barrel cortex. (Left) HT-GluA1 stained with JF_{549i}-HTL. (Middle) PSD95 (PSD95.FingR-eGFP) from same region of interest. (Right) Merge. Scale bars, 5 µm. **(d), (e)** Dendritic segments expressing **(d)** HT-GluA1 only or **(E)** PSD95.FingR-eGFP only. Scale bars, 2 µm. **(f)** Manders' overlap coefficient between HT-GluA1 and PSD95 (PSD95.FingR-eGFP). *n* = 9 dendritic segments from 5 neurons. Error bars show mean ± s.e.m. **(g)** Correlation between PSD95.FingR-eGFP intensity and HT-GluA1 intensity on individual spines (*n* = 112 spines from 8 dendritic segments from 8 neurons). *R*, Pearson's linear correlation coefficient, *P* value from two-sided Student's t-test. HT-GluA1 expressing layer 2/3 pyramidal neurons in barrel cortex in acute brain slices were identified by staining with 1uM JFX_{608}-HTL. **(h)** Representative patch-clamp recordings in acute brain slice. **(i)** Measurements of electrophysiological properties of neurons with or without HT-GluA1 expression. Membrane resistance: 204 ± 16 MΩ vs. 212 ± 12 MΩ, *P* = 0.69; membrane capacitance: 47 ± 5 pF vs. 43 ± 3 pF, *P* = 0.50; resting potential: −68.1 ± 1.4 mV vs. −69.2 ± 1.1 mV, *P* = 0.53; and rheobase 97 ± 9.8 pA vs. 94 ± 15 pA, *P* = 0.86 (*n* = 13 neurons for each group). Error bars show mean ± s.e.m. n.s. not significant, two-sided Student's t-test. Spine density on dendritic segments from neurons +/− HT-GluA1 in **(j)** layer 2/3 pyramidal neurons in barrel cortex and **(k)** pyramidal neurons in CA1 (HT-GluA1 (+) in barrel cortex: *n* = 11 dendritic segments from 10 neurons; HT-GluA1 (−) in barrel cortex: *n* = 11 dendritic segments from 11 neurons; HT-GluA1 (+) in CA1: *n* = 8 dendritic segments from 5 neurons; HT-GluA1 (−) in CA1: *n* = 8 dendritic segments from 4 neurons). Two-sided Wilcoxon rank-sum test. Error bars show mean ± s.e.m. **(l)** Confocal images of HT-GluA1 stained with JF_{549}-HTL (orange), co-expressed GPI-eGFP (green), and immunostained for GluA1 (red). Selected regions for quantifying GluA1 expression levels in neurons with HT-GluA1 (red) or without HT-GluA1 (yellow) are indicated on the GPI-eGFP panels. HT-GluA1 (+) and (−) regions were selected to be within 100 µm of each other, considering possible heterogenous immunostaining. Scale bars, 10 µm. **(m)** GluA1 expression level in HT-GluA1 +/− neurons (*n* = 10 neurons from 3 animals for each group). Two-sided Wilcoxon rank-sum test. Error bars show mean ± s.e.m.

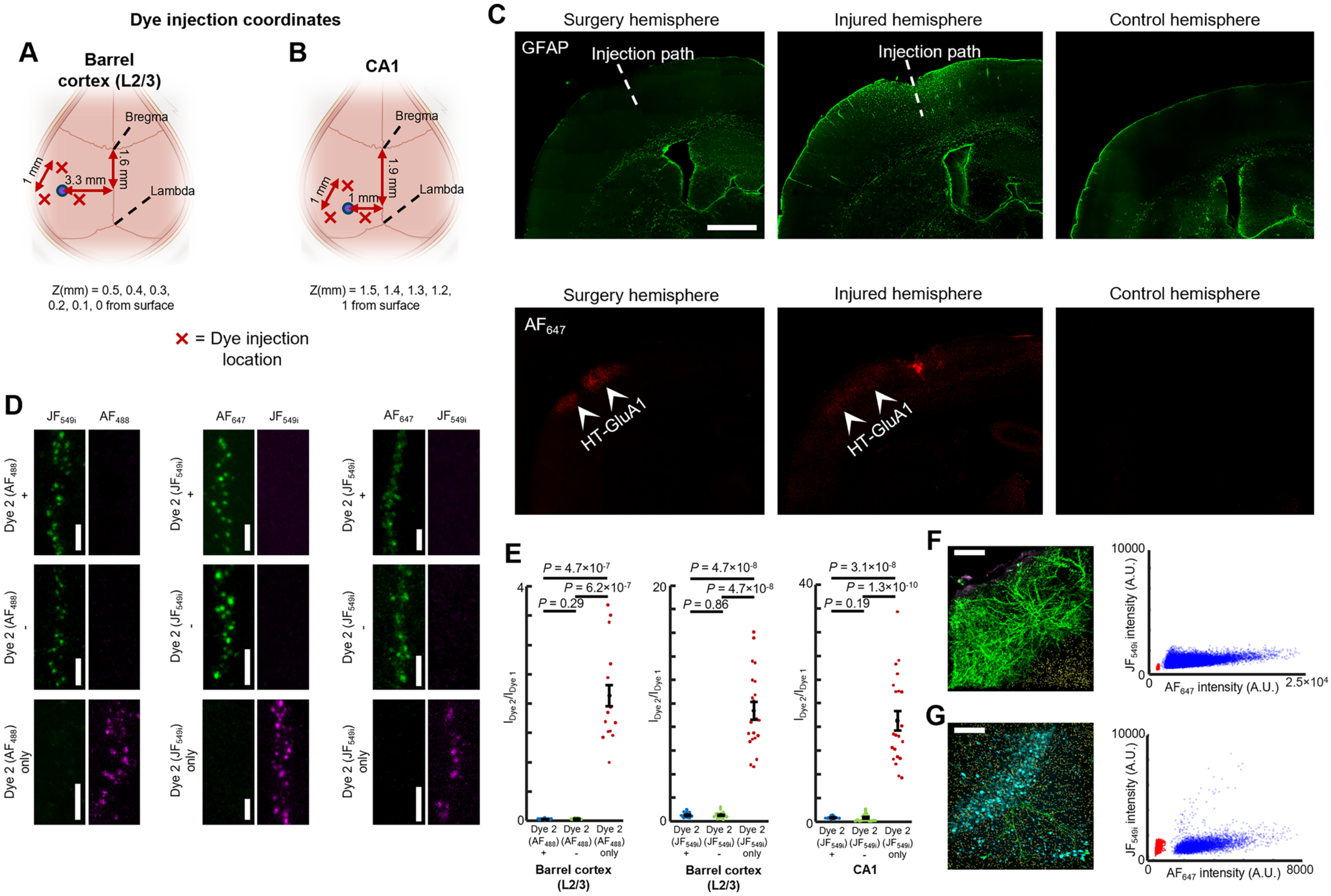

Extended Data Fig. 4 | HaloTag dye labeling in live mouse brain. (a) Relative coordinates from bregma and lambda for intracortical dye injections to cover layer 2/3 pyramidal neurons in left barrel cortex. **(b)** Relative coordinates from bregma and lambda for intrahippocampal dye injections to cover CA1 pyramidal neurons in left hippocampus. **(c)** Immunostaining of the astrocyte marker GFAP after dye injections. (Top) GFAP expression in the (top left) surgery hemisphere, (top middle) intentionally injured hemisphere, and (top right) control hemisphere without dye injection. (Bottom) HT-GluA1 stained with AF_{647}-HTL in the same regions of interest as the upper panels. 1 µM of AF_{647}-HTL was injected at three different sites as shown in **(a)** (80 nL at each depth) three times (20 minutes between the 1st and 2nd injections; 90 minutes between the 2nd and 3rd injections). Some of the injection paths are indicated by white dashed lines on the GFAP panels. These injections were performed 7 days after the installation of the injection port (see Methods). Each set of micrographs represents a single experiment from at least three repeated experiments. Scale bar, 1 mm. **(d)** Saturated labeling of surface GluA1 with Dye 1 blocked chase-dye labeling with Dye 2. Surface GluA1 was saturated by labeling with (left) 1 µM JF_{549i}-HTL for 20 minutes in layer 2/3 barrel cortex, (middle) 1 µM AF_{647}-HTL for 20 minutes in layer 2/3 barrel cortex, (right) 1 µM AF_{647}-HTL for 20 minutes in CA1. After Dye 1 labeling, 10 µM of Dye 2 was immediately injected to the same injection sites (Methods). Confocal images show Dye 1 (green) and Dye 2 (magenta) labeled dendrites (top) with Dye 2, (middle) without Dye 2, and (bottom) Dye 2 only. Scale bars, 5 µm. **(e)** Dye 2-to-Dye 1 intensity ratios for the injection conditions from **(d)**. *n* = 21 dendritic segments from 3 neurons, 20 dendritic segments from 3 neurons, 15 dendritic segments from 3 neurons for Dye 2 (+), Dye 2 (−), Dye 1 only groups in JF_{549i}/AF_{488} in barrel cortex, respectively; *n* = 21 dendritic segments from 3 neurons for each group in AF_{647}/JF_{549i} in barrel cortex; *n* = 21 dendritic segments from 3 neurons for each group in CA1. Error bars show mean ± s.e.m. Two-sided Student's t-test. **(f)** Background fluorescence analysis in mouse barrel cortex layer 2/3. Left: Spherical regions of interest (yellow) used for background fluorescence measurement on top of Fig. 2g. Right: Scatterplots of spine (blue) and background (red) fluorescence intensities (*n* = 53,457 spines and 747 background regions). **(g)** Background fluorescence analysis in mouse CA1. Left: Spherical regions of interest (yellow) used for background fluorescence measurement on top of Fig. 3c. Right: Scatterplots of spine (blue) and background (red) fluorescence intensities (*n* = 5,314 spines and 2,836 background regions). Scale bars: 200 µm. Schematics in **a** and **b** created using BioRender.com.

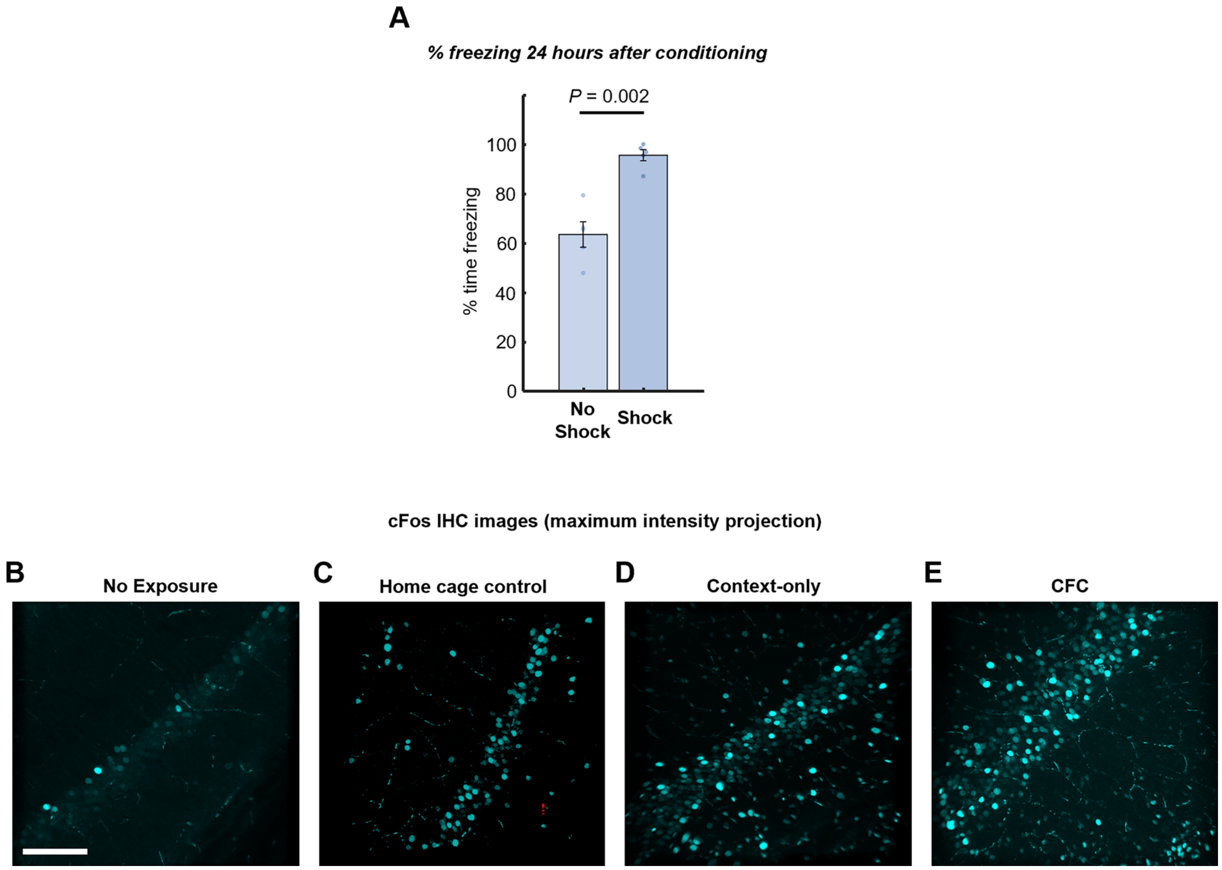

Extended Data Fig. 5 | Validation of contextual fear conditioning protocol. **(a)** The CFC system was validated by measuring the percent of time mouse spent freezing (that is immobile) 24 hours after conditioning. The percentage of freezing was measured for the mice that underwent full conditioning (shock) and for the mice exposed to the identical context but that did not receive an aversive stimulus (no shock). Error bars represent mean ± s.e.m. (*n* = 5 mice for each group). Two-sided Wilcoxon rank-sum test. Representative images from CA1 from mice that **(b)** were not exposed to any context (that is euthanized after 3 hours of anesthesia), **(c)** were not exposed to the novel context (stayed in their home cages, home cage control), **(d)** were exposed to the novel context but did not receive an aversive foot shock (context-only), and **(e)** underwent CFC. The images are shown in the same contrast scale and are maximum-intensity projections of z-stacks. These images are representative of the dataset used in Fig. 3m. Scale bars: 200 µm.

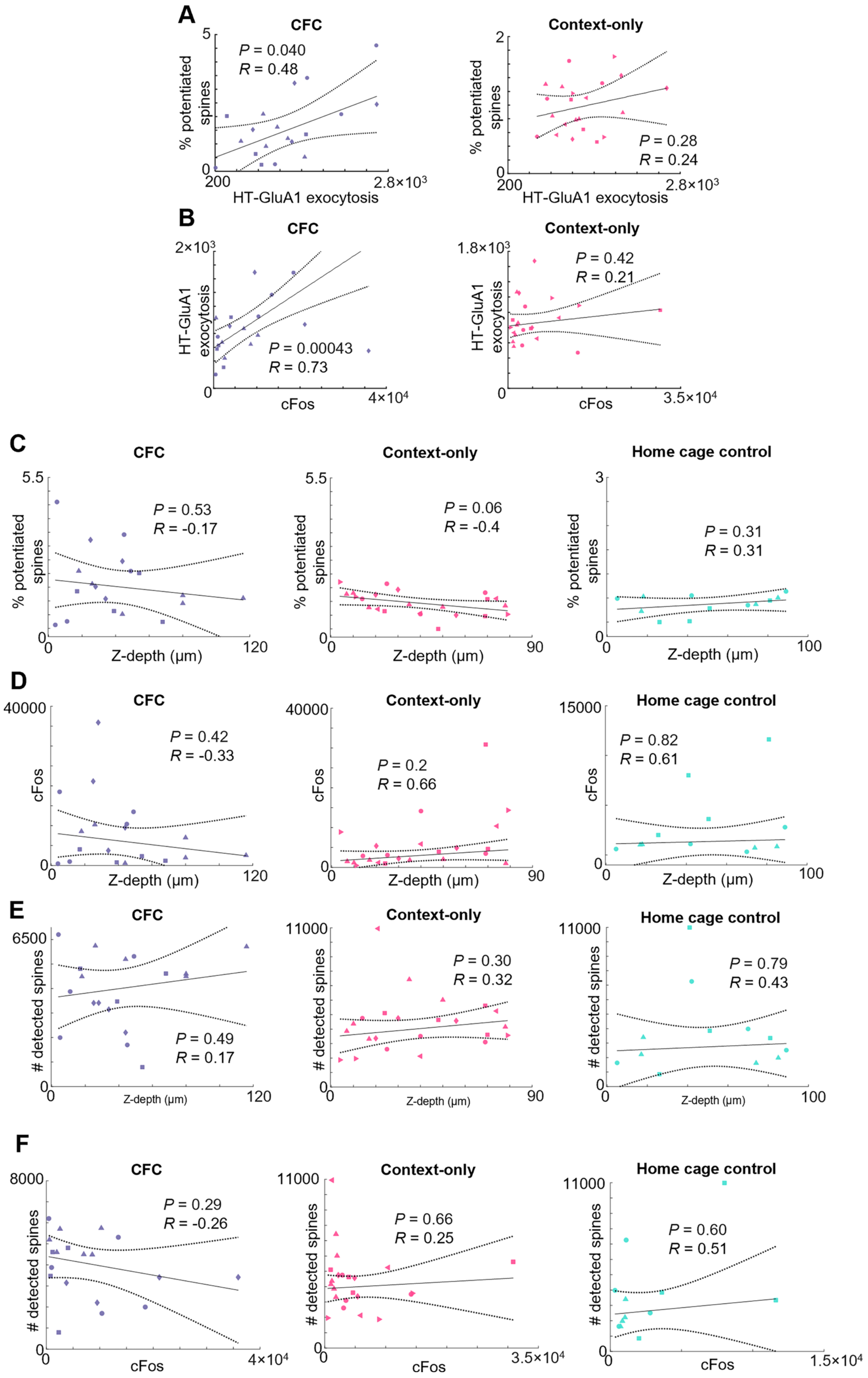

Extended Data Fig. 6 | See next page for caption.

Extended Data Fig. 6 | Relationships among cFos expression, AMPAR exocytosis levels, and percentage of potentiated spines. (a) Relation of the percentage of potentiated spines to the mean HT-GluA1 exocytosis among potentiated spines (distance of Dye 2 signal above threshold, averaged over above-threshold spines), for (left) CFC and (right) context-only control. **(b)** Relation between the mean HT-GluA1 exocytosis among potentiated spines and the corresponding cFos intensity. CFC: *n* = 19 cells from 4 animals; context-only: *n* = 22 cells from 6 animals. *R*, Pearson's linear correlation coefficient, *P* value from two-sided Student's t-test. Distinct animals represented by different shape symbols. **(c)** Relation between the percentage of potentiated spine and the z-coordinate of the center of soma of the corresponding neuron for (left) CFC, (middle) context-only control, and (right) home cage control. **(d)** Relation between cFos intensity and the z-coordinate of the center of soma of the corresponding neuron for (left) CFC, (middle) context-only control, and (right) home cage control. **(e)** Relation between the total number of identified spines and the z-coordinate of the center of soma of the corresponding neuron for (left) CFC, (middle) context-only control, and (right) home cage control. CFC: *n* = 19 cells from 4 animals; context-only: *n* = 23 cells from 6 animals; home cage control: *n* = 12 cells from 3 animals. *R*, Pearson's linear correlation coefficient, *P* value from two-sided Student's t-test. Distinct animals represented by different shape symbols. **(f)** Relation between the total number of identified spines and the cFos intensity of the corresponding neuron for (left) CFC, (middle) context-only control, and (right) home cage control. CFC: *n* = 19 cells from 4 animals; context-only: *n* = 23 cells from 6 animals; home cage control: *n* = 12 cells from 3 animals. *R*, Pearson's linear correlation coefficient, *P* value from two-sided Student's t-test. Distinct animals represented by different shape symbols.

https://doi.org/10.1038/s41593-025-01922-5

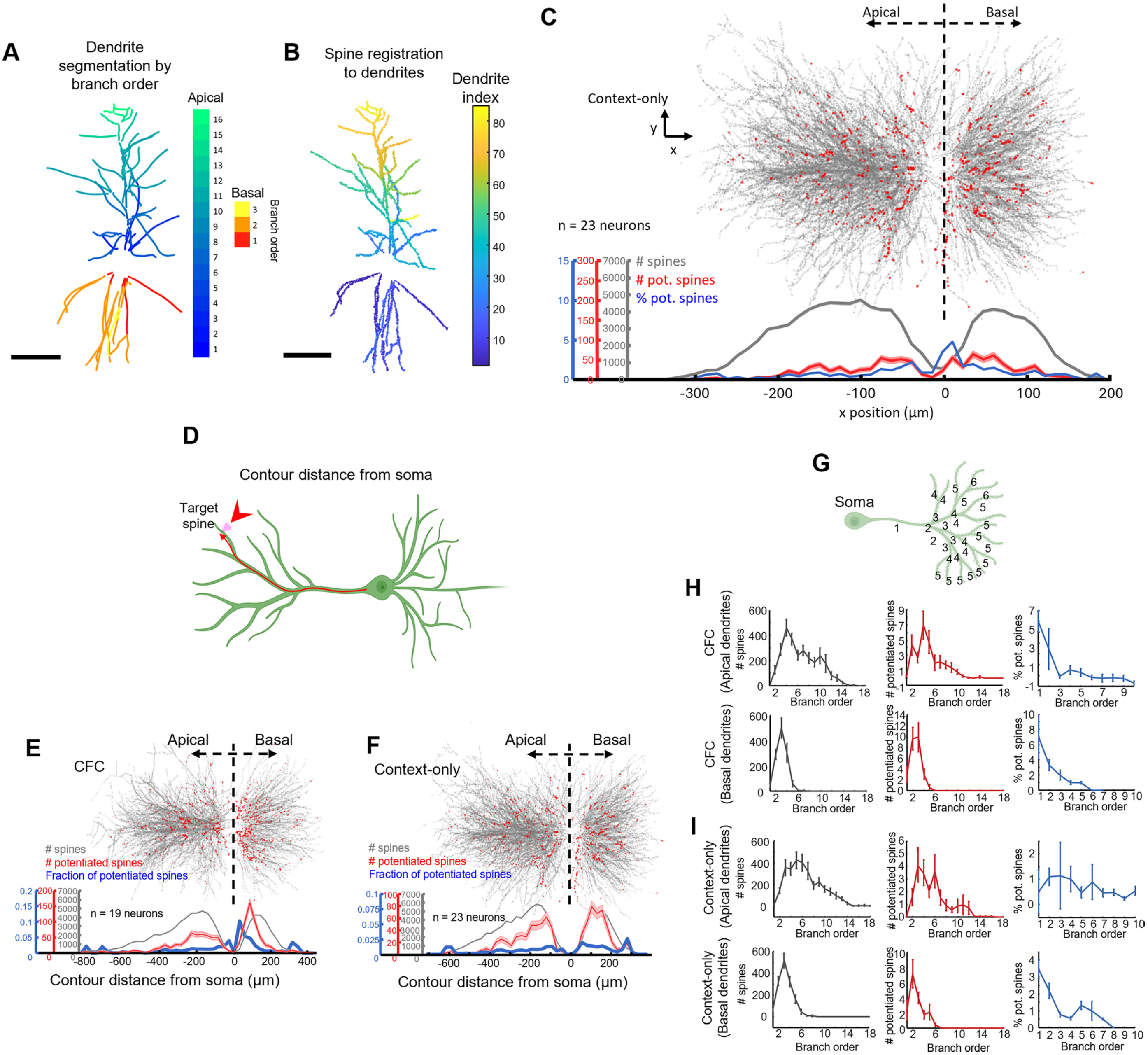

Extended Data Fig. 7 | Subcellular distribution of potentiated spines. **(a)** Representative neuron with dendrites segmented and colored by their branch order. **(b)** Same neuron with spines registered to the nearest segmented dendrites. Scale bars: 100 µm. **(c)** Distribution of potentiated spines as a function of projected distance from the *stratum pyramidale*. (Top) Overlapped images of all identified spines (gray) and spines with high HT-GluA1 exocytosis (red) from the context-only control group. (Bottom) Total number of identified spines (grey), number of spines with high HT-GluA1 exocytosis (red), and fraction of potentiated spines (blue) plotted against the projected distance from the *stratum pyramidale* (x-axis from the top panel). Error bars represent count ± square root(count). **(d)** Schematic diagram showing the contour distance of a neuron's spine from its soma. This is the distance along the dendrite backbone. **(e, f)** Same data as in Fig. 4a and (**c**), but plotted vs. contour distance instead of *x*. **(g)** Schematic drawing of a neuron with dendrites numbered by their branch order. **(h), (i)** Total number of identified spines (left), number of potentiated spines (middle), fraction of potentiated spines (right) vs. corresponding dendrites' branch order from (top) apical dendrites or (bottom) basal dendrites in **(h)** CFC group and **(i)** context-only controls. CFC: $n = 19$ neurons; context-only: $n = 23$ neurons. Data are represented as mean ± s.e.m. The right panels are truncated due to the division by small numbers of spines on branch orders greater than 10. Schematics in **d** and **g** created using BioRender.com.

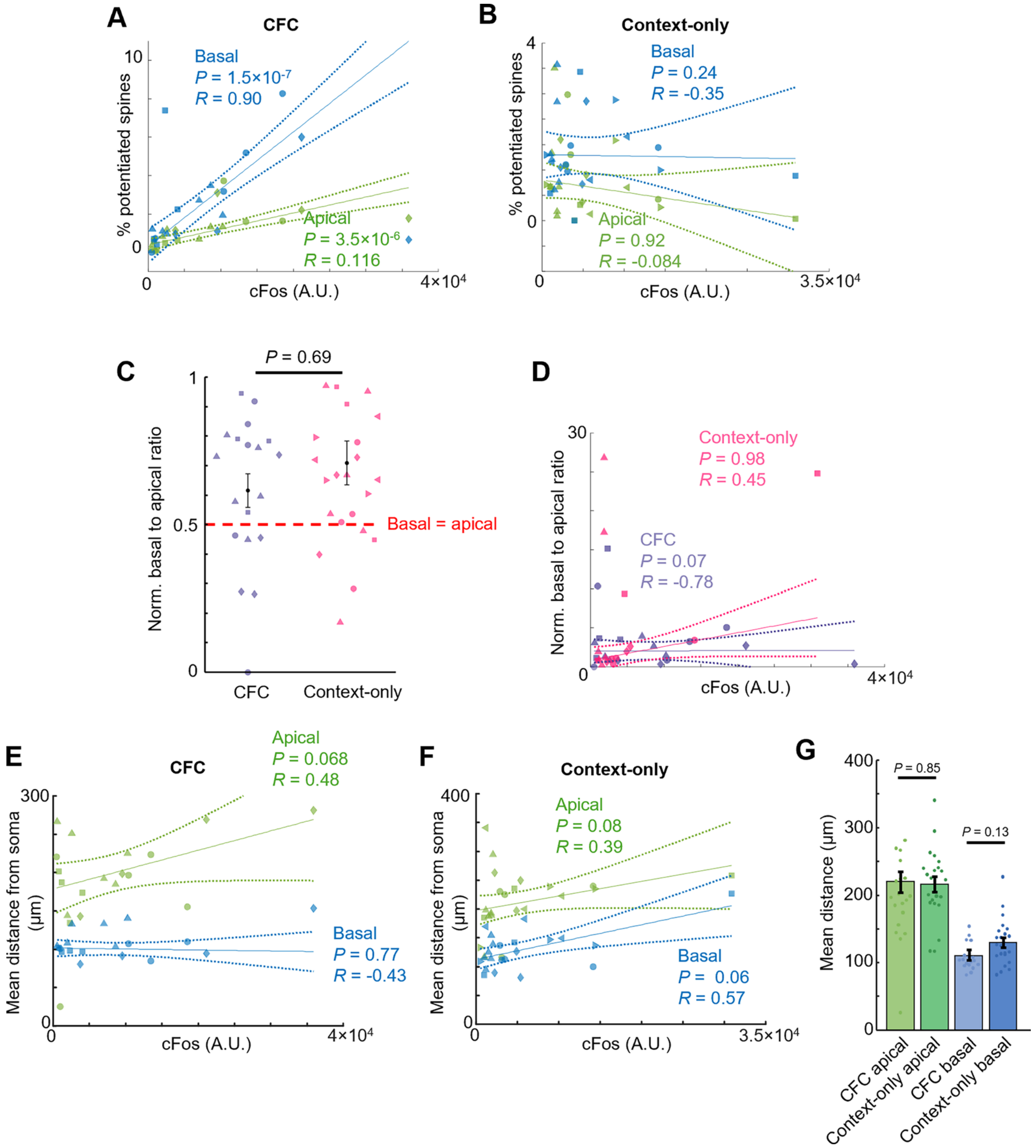

Extended Data Fig. 8 | Comparison of AMPAR exocytosis in basal vs. apical dendrites. Fraction of potentiated spines for each neuron vs. cFos intensity for **(a)** CFC (n = 19 neurons) and **(b)** context-only control (n = 23 neurons). Spine fraction was separately evaluated for basal and apical dendrites. **(c)** Normalized basal to apical ratio of percent potentiated spines. Normalized ratio: basal percent potentiated spines / (basal percent potentiated spines + apical percent potentiated spines). 13 of 19 neurons in the CFC group and 17 of 23 neurons in the context-only group had higher basal than apical fraction of potentiated spines. There was no significant difference between the CFC and context-only groups in the ratio of basal to apical potentiated spines (CFC: 0.61 ± 0.06, mean ± s.e.m.; context-only: 0.70 ± 0.07, mean ± s.e.m.). Two-sided Wilcoxon rank-sum test. **(d)** Basal to apical ratio of percent potentiated spines vs. cFos intensity. The basal to apical ratio was not correlated with the corresponding cFos levels. R, Pearson's linear correlation coefficient, P value from two-sided Student's t-test. Distinct mice represented by different shape symbols. Mean contour distance from soma to potentiated spines vs. corresponding cFos intensity for **(e)** CFC group and **(f)** context-only control. The mean distance was separately evaluated for spines in basal and apical dendrites. R, Pearson's linear correlation coefficient, P value from two-sided Student's t-test. Distinct mice represented by different shape symbols. **(g)** Mean contour distance from soma to potentiated spines in CFC and context-only group. Data are represented as mean ± s.e.m. Two-sided Wilcoxon rank-sum test. CFC: n = 19 neurons; context-only: n = 22 neurons.

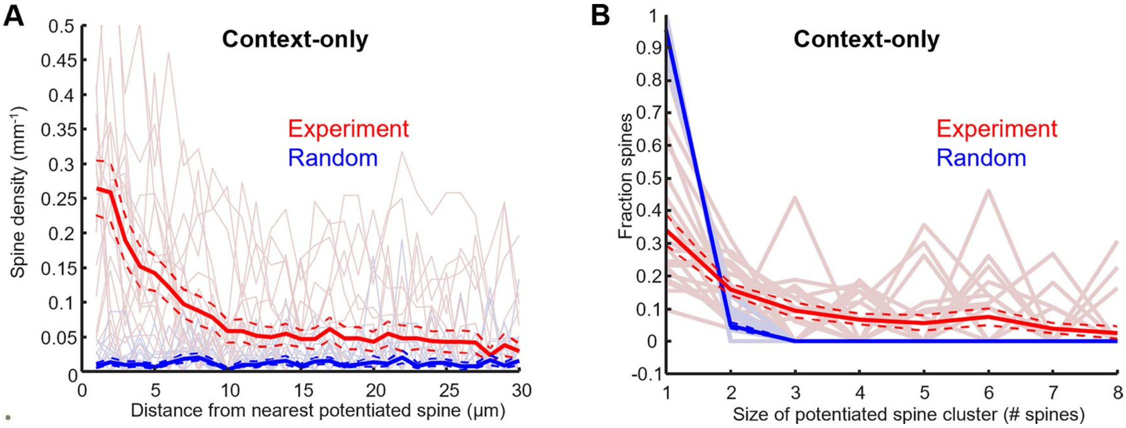

Extended Data Fig. 9 | Clustering of potentiated spines in context-only control. **(a)** Density profile of potentiated spines as a function of distance from the nearest potentiated spine. The single-cell profiles are plotted with light colors. Random: simulation where the same number of potentiated spines are distributed randomly and independently among all detected spines. Bold and dashed lines represent mean ± s.e.m. **(b)** Fraction of potentiated spine clusters of different sizes from the context-only group (*n* = 22 neurons). The single-cell profiles are plotted with light colors. Bold and dashed lines represent mean ± s.e.m. Random defined as in **(a)**.

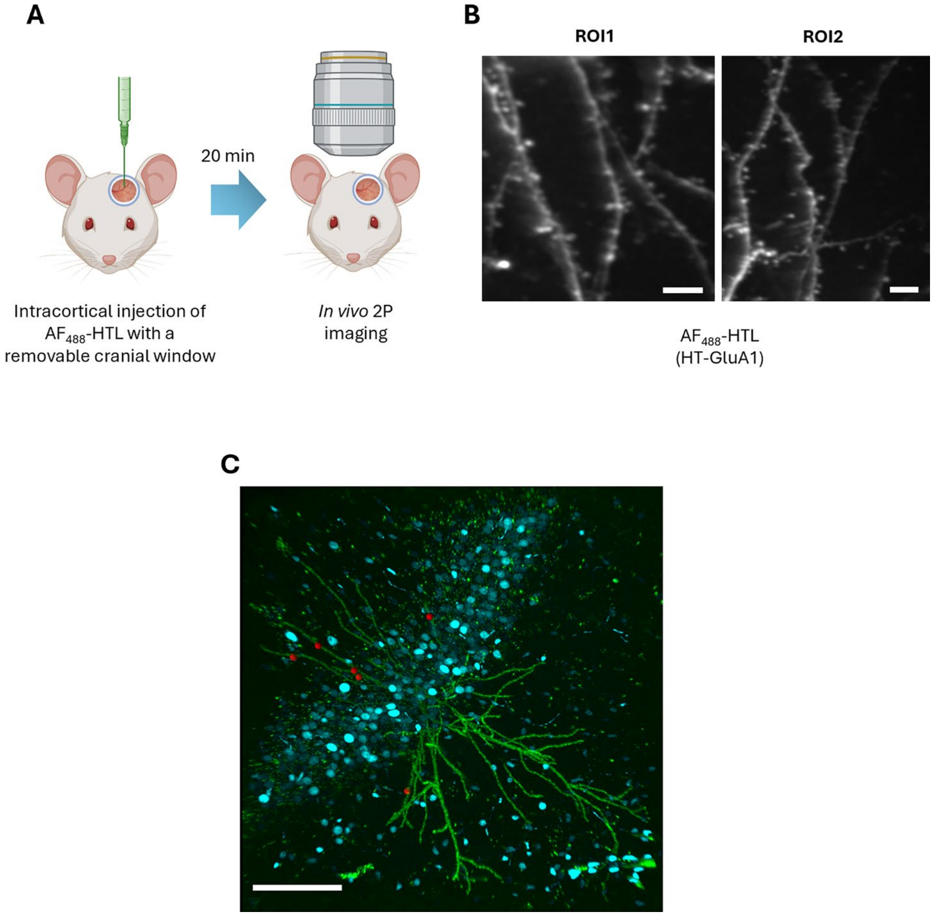

Extended Data Fig. 10 | Possible extensions of the EPSILON technique. **(a,b)** Monitoring spine dynamics *in vivo*. **(a)** Experimental setup for intracortical injection of membrane-impermeable AF_{488}-HTL dye into mouse barrel cortex expressing HT-GluA1, followed by *in vivo* 2-photon imaging. **(b)** Representative *in vivo* 2-photon images of layer 2/3 pyramidal neuron apical tuft dendrites and spines stained with AF_{488}-HTL. This set of micrographs represents a single experiment. Scale bars, 5 µm. **(c)** Detecting new spine formation. New spines are expected to be labeled only with Dye 2, not Dye 1. Locations of the spines labeled with Dye 2 only are indicated with red dots. Neuron from Fig. 3c. This micrograph represents a single experiment. See Methods for the detection of Dye 2 only spines. Scale bar, 200 µm. Schematic in **a** created using BioRender.com.

nature portfolio

Corresponding author(s): Adam E. Cohen

Last updated by author(s): Jan 15, 2025

Reporting Summary

Nature Portfolio wishes to improve the reproducibility of the work that we publish. This form provides structure for consistency and transparency in reporting. For further information on Nature Portfolio policies, see our Editorial Policies and the Editorial Policy Checklist.

Statistics

For all statistical analyses, confirm that the following items are present in the figure legend, table legend, main text, or Methods section.

n/a	Confirmed	
☐	☒	The exact sample size (*n*) for each experimental group/condition, given as a discrete number and unit of measurement
☐	☒	A statement on whether measurements were taken from distinct samples or whether the same sample was measured repeatedly
☐	☒	The statistical test(s) used AND whether they are one- or two-sided *Only common tests should be described solely by name; describe more complex techniques in the Methods section.*
☐	☒	A description of all covariates tested
☐	☒	A description of any assumptions or corrections, such as tests of normality and adjustment for multiple comparisons
☐	☒	A full description of the statistical parameters including central tendency (e.g. means) or other basic estimates (e.g. regression coefficient) AND variation (e.g. standard deviation) or associated estimates of uncertainty (e.g. confidence intervals)
☐	☒	For null hypothesis testing, the test statistic (e.g. *F*, *t*, *r*) with confidence intervals, effect sizes, degrees of freedom and *P* value noted *Give P values as exact values whenever suitable.*
☒	☐	For Bayesian analysis, information on the choice of priors and Markov chain Monte Carlo settings
☒	☐	For hierarchical and complex designs, identification of the appropriate level for tests and full reporting of outcomes
☐	☒	Estimates of effect sizes (e.g. Cohen's *d*, Pearson's *r*), indicating how they were calculated

Our web collection on statistics for biologists contains articles on many of the points above.

Software and code

Policy information about availability of computer code

Data collection	The confocal imaging data were acquired with Zeiss ZEN (blue edition).
Data analysis	The data were analyzed with Imaris (9-10), Fiji, and MATLAB (2019-2021). Description of these methods are reported in the Methods section and Supplementary Information. The code involved custom scripts that included standard image processing steps, written specifically for the datasets, without any novel algorithms.

For manuscripts utilizing custom algorithms or software that are central to the research but not yet described in published literature, software must be made available to editors and reviewers. We strongly encourage code deposition in a community repository (e.g. GitHub). See the Nature Portfolio guidelines for submitting code & software for further information.

Data

Policy information about availability of data

All manuscripts must include a data availability statement. This statement should provide the following information, where applicable:

- Accession codes, unique identifiers, or web links for publicly available datasets
- A description of any restrictions on data availability
- For clinical datasets or third party data, please ensure that the statement adheres to our policy

All data, including images of dye-stained HT-GluA1-expressing neurons and patch-clamp recordings, are available from the corresponding author upon reasonable request.

Research involving human participants, their data, or biological material

Policy information about studies with human participants or human data. See also policy information about sex, gender (identity/presentation), and sexual orientation and race, ethnicity and racism.

Reporting on sex and gender	N/A
Reporting on race, ethnicity, or other socially relevant groupings	N/A
Population characteristics	N/A
Recruitment	N/A
Ethics oversight	N/A

Note that full information on the approval of the study protocol must also be provided in the manuscript.

Field-specific reporting

Please select the one below that is the best fit for your research. If you are not sure, read the appropriate sections before making your selection.

☒ Life sciences ☐ Behavioural & social sciences ☐ Ecological, evolutionary & environmental sciences

For a reference copy of the document with all sections, see nature.com/documents/nr-reporting-summary-flat.pdf

Life sciences study design

All studies must disclose on these points even when the disclosure is negative.

Sample size	Sample sizes were determined by the technical requirements of the experiments. Experiments were replicated on as many cells, dendrites, and animals as practical. Sample sizes were not pre-defined. Statistical analyses were performed to account for technical and biological variability.
Data exclusions	Confocal images were acquired and analyzed for neurons where soma and dendrites were visible and connected.
Replication	For in vitro (cultured neuron) experiments, 5 or more cells were used in each experiment. For in vivo experiments, 3 or more animals were used in each experiment. All acquired datasets are presented in the manuscript.
Randomization	Allocation of individual samples into control and experimental groups was done randomly. For in vitro (cultured neuron) experiments, cultured dishes from the same batch were randomly selected for different experimental conditions from the incubator. For in vivo experiments, animals from the same in utero electroporation batch were randomly selected for different experimental conditions. Individual animals were indistinguishable in terms of HT-GluA1 expression status at the time of the experiments.
Blinding	For data collection, blinding was not practical because the same person performed the surgery and data acquisition. However, all confocal images were acquired with a same set of parameters as indicated in the Methods section. All analysis was performed iteratively and identically over individual samples using fully automated software with a same set of parameters, and hence was blinded.

Reporting for specific materials, systems and methods

We require information from authors about some types of materials, experimental systems and methods used in many studies. Here, indicate whether each material, system or method listed is relevant to your study. If you are not sure if a list item applies to your research, read the appropriate section before selecting a response.

Materials & experimental systems

n/a	Involved in the study	
☐	☒	Antibodies
☐	☒	Eukaryotic cell lines
☒	☐	Palaeontology and archaeology
☐	☒	Animals and other organisms
☒	☐	Clinical data
☒	☐	Dual use research of concern
☒	☐	Plants

Methods

n/a	Involved in the study	
☒	☐	ChIP-seq
☒	☐	Flow cytometry
☒	☐	MRI-based neuroimaging

Antibodies

Antibodies used	rat anti-cFos primary antibody (Synaptic Systems, 226 017), AF488 anti-rat secondary antibody, (Invitrogen, A-11006), mouse anti-GluA1 CTD primary antibody (Synaptic Systems, 182 011), AF647 anti-mouse secondary antibody (Abcam, A-150115), rabbit anti-GFAP primary antibody (Abcam, 7260), AF488 anti-rabbit secondary antibody (Invitrogen A-11008)
Validation	According to the vendors, these antibodies were verified by relative expression to ensure they bind to the stated antigens. Specifically, Synaptic Systems 226 017, 182 011, and Abcam 7260 primary antibodies were validated by immunoprecipitation (using mouse lysate), as per the vendors' specifications.

Eukaryotic cell lines

Policy information about cell lines and Sex and Gender in Research

Cell line source(s)	HEK293T ATCC CRL-3216
Authentication	The cell line was tested by ATCC with the STR profiling
Mycoplasma contamination	All cell lines were tested negative of mycoplasma
Commonly misidentified lines (See ICLAC register)	None

Animals and other research organisms

Policy information about studies involving animals; ARRIVE guidelines recommended for reporting animal research, and Sex and Gender in Research

Laboratory animals	Acute slice patch clamp experiments were performed in CD-1 IGS mice of postnatal day 14 - 16. For all other experiments, C57BL/6 and CD-1 IGS mice between 8-12 postnatal weeks were used. All mice were housed in standard conditions (reverse 12-hour light/dark cycles, with water and food ad libitum).
Wild animals	No wild animals were used in this study.
Reporting on sex	Both sexes were used without discrimination.
Field-collected samples	No field-collected samples were used in this study.
Ethics oversight	All animal procedures adhered to the National Institutes of Health Guide for the care and use of laboratory animals and were approved by the Harvard University Institutional Animal Care and Use Committee (IACUC).

Note that full information on the approval of the study protocol must also be provided in the manuscript.

Plants

Seed stocks	N/A
Novel plant genotypes	N/A
Authentication	N/A